

THE FIRST DETECTIONS OF THE EXTRAGALACTIC BACKGROUND LIGHT AT 3000, 5500, AND 8000 Å. III. COSMOLOGICAL IMPLICATIONS

REBECCA A. BERNSTEIN,^{1,2,3} WENDY L. FREEDMAN,² AND BARRY F. MADORE^{2,4}

Received 2000 June 11; accepted 2002 January 2

ABSTRACT

We have used the *Hubble Space Telescope* Wide Field and Planetary Camera 2 in combination with ground-based spectroscopy to measure the integrated flux of galaxies at optical wavelengths—the extragalactic background light (EBL). We have also computed the integrated light from individual galaxy counts in the images used to measure the EBL and in the Hubble Deep Field. We find that flux in galaxies as measured by standard galaxy photometry methods has generally been underestimated by about 50%, resulting from missed flux in the outer, lower surface brightness parts of galaxies and from associated errors in the estimated sky level. Comparing the corrected, integrated flux from individual galaxies with our total EBL measurement, we find that there is yet further light that contributes to the background that is not represented by galaxy counts and that the total flux in individually detected sources is a factor of 2–3 less than the EBL from 8000 to 3000 Å. We show that a significant fraction of the EBL may come from normal galaxies at $z < 4$, which are simply undetectable as a result of K -corrections and cosmological surface brightness dimming. This result is consistent with results from recent redshift surveys at $z < 4$. In the context of some simple models, we discuss the constraints placed by the EBL on evolution in the luminosity density at $z > 1$; while significant flux comes from galaxies beyond the current detection limits, this evolution cannot be tightly constrained by our data. Based on our measurements of the optical EBL, combined with previously published measurements of the UV and IR EBL, we estimate that the total EBL from 0.1 to 1000 μm is $100 \pm 20 \text{ nW m}^{-2} \text{ sr}^{-1}$. If the total EBL were produced entirely by stellar nucleosynthesis, then we estimate that the total baryonic mass processed through stars is $\Omega_* = 0.0062(\pm 0.0022) h^{-2}$ in units of the critical density. For currently favored values of the baryon density Ω_B this corresponds to $0.33 \pm 0.12 \Omega_B$. This estimate is smaller by roughly 7% if we allow for a contribution of $7 h_{0.7} \text{ nW m}^{-2} \text{ sr}^{-1}$ to the total EBL from accretion onto central black holes. This estimate of Ω_* suggests that the universe has been enriched to a total metal mass of $0.21 (\pm 0.13) Z_\odot \Omega_B$, which is consistent with other observational estimates of the cumulative metal mass fraction of stars, stellar remnants, and the intracluster medium of galaxy clusters in the local universe.

Subject headings: cosmology: observations — diffuse radiation — galaxies: evolution — galaxies: photometry

1. INTRODUCTION

The integrated optical flux from all extragalactic sources is a record of the stellar nucleosynthesis in the universe and the chemical evolution that has resulted from it. In Bernstein, Freedman, & Madore (2002a, hereafter Paper I), we presented detections of the optical extragalactic background light (EBL) in the *Hubble Space Telescope* (*HST*) Wide Field Planetary Camera 2 (WFPC2) wideband filters F300W (U_{300} , $\lambda_0 \sim 3000$ Å), F555W (V_{555} , $\lambda_0 \sim 5500$ Å), and F814W (I_{814} , $\lambda_0 \sim 8000$ Å) based on simultaneous data sets from *HST* and the Las Campanas Observatory (LCO). In Bernstein, Freedman, & Madore (2002b, hereafter Paper II), we presented details of a measurement of the diffuse foreground zodiacal light that we use in Paper I. Here we briefly summarize the results of Papers I and II and discuss the cosmological implications of these detections of the EBL.

The majority of the EBL at UV to IR wavelengths is produced by stars at rest-frame wavelengths of 0.1–10 μm . Because of cosmic expansion, the EBL at U_{300} , V_{555} , and I_{814} potentially includes redshifted light from stellar populations out to $z \sim 8$ (the redshifted Lyman limit cutoff of the I_{814} filter). Although stars themselves do not emit much light at wavelengths longer than 10 μm , a complete census of the energy produced by stellar nucleosynthesis in the universe must consider the EBL over the full wavelength range 0.1–1000 μm because dust in the emitting galaxies will absorb and reradiate starlight, redistributing energy from nucleosynthesis into the thermal IR.

With 8 m class telescopes and *HST*, the limits of resolved-source methods (i.e., number counts, redshift surveys, quasar [QSO] absorption lines, etc.) for studying star formation in the universe are being extended to ever fainter levels; however, a direct measurement of the EBL remains an invaluable complement to these methods. Galaxies with low *apparent* surface brightness—both intrinsically low surface brightness galaxies at low redshift and normal surface brightness galaxies at high redshift—are easily missed in surface brightness-limited galaxy counts and, consequently, in follow-up redshift surveys. Identification, not to mention photometry, of faint galaxies becomes very uncertain near the detection limits. Even efforts to understand galaxy evolution, chemical enrichment, and star formation through

¹ Division of Math, Physics, and Astronomy, California Institute of Technology, MS 103-33, Pasadena, CA 91125; rab@ociw.edu.

² Carnegie Observatories, 813 Santa Barbara Street, Pasadena, CA 91101.

³ Hubble Fellow.

⁴ NASA/Infrared Processing and Analysis Center Extragalactic Database, California Institute of Technology, MS 100-22, 770 South Wilson Avenue, Pasadena, CA 91125.

QSO absorption line studies appear to be biased against chemically enriched, dustier systems since these systems can obscure QSOs that might lie behind them (Fall & Pei 1989; Pei & Fall 1995; Pettini et al. 1999). In contrast, a direct measurement of the spectral energy distribution (SED) of the EBL from the UV to the far-IR is a complete record of the energy produced by star formation and is immune to surface brightness selection effects.

In addition to energy originating from stellar nucleosynthesis, the EBL includes energy emitted by accreting black holes in QSOs and active galactic nuclei. However, at optical wavelengths, the QSO luminosity functions at redshifts $z \lesssim 5$ indicate that the optical luminosity density from QSOs is a small fraction ($\sim 2.5\%$) of that from galaxies (see, e.g., Boyle & Terlevich 1998). In addition, our measurement of the EBL excludes any pointlike sources (of which there are three in our images) under the prior assumption that those sources are Galactic foreground stars. We therefore expect QSOs to be a negligible source of flux in our measurements of the optical EBL.

The contribution from active galactic nuclei (AGNs) is more difficult to assess since recent dynamical evidence (Richstone et al. 1998) indicates that massive black holes reside in most galaxies, and sensitive optical spectroscopy (Ho, Filippenko, & Sargent 1997a, 1997b) indicates that AGNs have at least a weak contribution to more than 50% of nearby galaxies. Nonetheless, simple accretion models, the total X-ray background, and the X-ray-to-far-IR spectral energy distribution of AGNs and QSOs all indicate that the total contribution to the bolometric EBL from accretion onto central black holes is $\lesssim 15\%$ (see § 6.2) and is emitted at thermal IR wavelengths. In principle, measurements of the EBL also constrain the total energy output from more exotic sources, such as gravitationally collapsing systems, brown dwarfs, and decaying particles (see Bond, Carr, & Hogan 1986, 1991 and Dwek et al. 1998 for discussions).

The outline of the paper is as follows: In § 2 we give an overview of the observations and methods used to measure the EBL, as discussed in Papers I and II. In § 3 we summarize the individual measurements and associated errors we have obtained from each data set and the final EBL detections that result from them. In § 4 we compare the measured EBL with the integrated optical flux from resolvable sources as quantified by number counts and luminosity functions. In § 5 we quantify the contributions to the optical EBL that one might expect from sources that fall below the detection limits of the Hubble Deep Field (HDF) based on explicit assumptions regarding the surface brightness, luminosity, and redshift distribution of galaxy populations in the universe. In § 6 we discuss models of the EBL SED based on these and recent results in the far-infrared. Finally, in § 7 we discuss the total star formation and chemical enrichment history of the universe required to produce the bolometric flux of the EBL and compare the inferred values to other observations of the total baryon fraction in stars and the metal mass density in the local universe. We abbreviate the adopted units of $\text{ergs s}^{-1} \text{cm}^{-2} \text{sr}^{-1} \text{\AA}^{-1}$ as cgs throughout.

2. SUMMARY OF OBSERVATIONS

As is true of all background measurements, the difficulty in measuring the optical EBL is in differentiating it from the much brighter foregrounds: terrestrial airglow, zodiacal light (ZL), and diffuse Galactic light (DGL). Relative to the

EBL flux at $\sim 5000 \text{\AA}$, airglow and ZL are each more than 100 times brighter than the EBL. Along the most favorable lines of sight, the DGL is roughly equal in flux to the EBL. We have measured the EBL in a field that is out of the ecliptic plane and near the Galactic pole in order to optimally minimize the contributions of zodiacal light, DGL, and nearby stars (see Paper I).

In the EBL measurement presented in Paper I, we have used three simultaneous data sets to isolate the diffuse EBL from the foreground sources: (1) absolute surface photometry taken with WFPC2 on board *HST* using the wideband filters F300W (U_{300}), F555W (V_{555}), and F814W (I_{814}), (2) low-resolution ($\sim 300 \text{\AA}$) surface spectrophotometry at 4000–7000 \AA taken with the Faint Object Spectrograph (FOS), also on board *HST*, and (3) moderate-resolution ($\sim 2 \text{\AA}$) surface spectrophotometry taken with the Boller & Chivens Spectrograph on the 2.5 m du Pont Telescope at LCO. We use the two *HST* data sets to measure the total mean flux of the night sky, including ZL, DGL, and the EBL. We avoid terrestrial airglow all together by using *HST* for this measurement. We then use the LCO spectra to measure the absolute surface brightness of ZL in the same field and on the same nights as the *HST* observations. Finally, we estimate the small DGL contribution using a scattering model that is in good agreement with the observations. We then subtract the measured ZL and the modeled DGL from the total flux measured with *HST*/WFPC2 through each filter and with *HST*/FOS. These measurements are described in detail in Papers I and II. Below, we summarize the observations, results, and accuracy of the individual measurements that contribute to the EBL detection (see Table 1).

Bright galaxies are not statistically well sampled in the 4.4 arcmin² WFPC2 field of view. We have, therefore, masked out any sources brighter than $V_{555} = 23$ AB mag in the WFPC2 images before we measured the total sky flux. To do so, we used masks that are derived from the F555W images and extend to 4 times the isophotal radius in those data. We use the abbreviation *EBL23* as a reminder of this bright magnitude cutoff. The EBL23 detections can be combined with ground-based counts at $V_{555} < 23$ AB mag to obtain the total EBL. The WFPC2 surface brightness measurements have random errors of less than 1% and systematic uncertainties of 1%–2% of the total background flux. From the *HST*/WFPC2 data alone, we can also identify a minimum flux from detectable sources. This minimum is given in Table 1, and the method used to obtain this result is summarized in § 3.

The FOS spectra also provide a measurement of total flux. The random error per resolution element is around 2.1%, and the systematic uncertainty over the full range is 3.5%. The ~ 14 arcsec² FOS field of view and $\sim 4\%$ systematic uncertainty make the FOS less useful than the WFPC2 for measuring the EBL. However, most of the systematic uncertainty is due to the poorly constrained solid angle of the aperture and aperture correction. Both of these are wavelength-independent errors so that the FOS spectra do provide a $\pm 1\%$ measurement of the color of the total background, which is dominated by zodiacal light.

The scattering that produces the ZL is well described by classical Mie theory for the large ($> 10 \mu\text{m}$), rough dust grains that populate the zodiacal dust cloud. The scattering efficiency of the dust is only weakly wavelength-dependent, so that the solar spectral features are well preserved in the

TABLE 1
SUMMARY OF MEASUREMENTS

Source	Bandpass	Data Source	Flux	Random (%)	Systematic (%)
Total background	F300W	<i>HST</i> /WFPC2	33.5	(±4.9)	[±5.6]
	F555W	<i>HST</i> /WFPC2	105.7	(±0.3)	[±1.4]
	F814W	<i>HST</i> /WFPC2	72.4	(±0.2)	[±1.4]
	F555W ^a	<i>HST</i> /FOS	111.5	(±0.7)	[±2.8]
Zodiacal light	4600–4700 Å	LCO	109.4	(±0.6)	[±1.1]
	F300W	LCO ^b	28.5	(±0.6)	[−1.1, 1.2]
	F555W	LCO ^b	102.2	(±0.6)	[−1.1, 1.1]
	F814W	LCO ^b	69.4	(±0.6)	[−1.3, 1.1]
Diffuse Galactic light	F300W	DGL model	1.0	...	[25, −50]
	F555W	DGL model	0.8	...	[25, −50]
	F814W	DGL model	0.8	...	[25, −50]

NOTE.—All fluxes are in units of 1×10^{-9} ergs s^{-1} cm^{-2} sr^{-1} \AA^{-1} . For a source with constant flux in F_λ , filters F300W, F555W, and F814W have effective wavelengths $\lambda_0(\Delta\lambda) = 3000(700)$, 5500 (1200), and 8000 (1500) Å, respectively. Individual sources of error contributing to each measurement are summarized in Tables 3 and 4 of Paper I and Table 1 of Paper II.

^a Observed FOS spectrum, convolved with the WFPC2/F555W bandpass to allow direct comparison with the WFPC2 results.

^b The LCO measurement of zodiacal light has been extrapolated to the WFPC2 bandpass by applying a correction for changing zodiacal light color with wavelength relative to the solar spectrum. The zodiacal light flux through the WFPC2 bandpasses was identified using SYNPHOT models, the uncertainty due to which is included in the uncertainty for the filter calibration and is shared with the systematic uncertainty for the total background flux.

scattered ZL spectrum. However, the broadband spectrum of the zodiacal light is redder than the solar spectrum by about 5% per 1000 Å (see Paper II for further discussion) because of surface roughness of the grains, which decreases scattering efficiency at shorter wavelengths. The mean ZL flux in a narrow band can thus be measured from the apparent equivalent width of the solar Fraunhofer lines evident in its spectrum. Small color corrections can then be used to infer the full spectrum relative to that measurement. This requires moderate-resolution spectra (~ 2 Å) with excellent flux calibration ($\pm 1\%$), which can only be obtained with ground-based observations and then only at wavelengths where atmospheric emission lines are relatively weak. We have, therefore, measured the ZL in the range 4000–5100 Å using spectra taken at LCO. The resulting measurement has a statistical error of less than 1% and a systematic uncertainty of $\sim 1.2\%$. This measurement has been extrapolated the 3000 and 8000 Å WFPC2 bandpasses using measurements of the color of the ZL from the FOS and ground-based LCO data.

Within the Galaxy, there is both resolved flux from discrete stars and diffuse light (DGL) from starlight scattered by interstellar dust. Discrete stars can simply be resolved and subtracted in the WFPC2 images. The intensity of the dust-scattered optical DGL and the 100 μm thermal emission from the same dust are both proportional to the dust column density and the strength of the interstellar radiation field. To minimize the optical DGL, our field was selected to have very low 100 μm emission. The remaining low-level DGL that does contribute has been estimated using a simple scattering model based on the dust column density and interstellar radiation field along the line of sight and empirical scattering characteristics for interstellar dust. The predictions of this model are in good agreement with observations of the DGL from 2500 to 9000 Å (see Witt, Friedmann, & Sasseen 1997 and references therein). Finally, although isotropic line emission from warm interstellar gas

is measured at all Galactic latitudes, the strongest line, $H\alpha$, does not lie within any of our *HST*/WFPC2 bandpasses. The next strongest lines, [O III], are 20 times weaker and contribute negligibly to our results.

The EBL cannot be measured in typical *HST* data. Our *HST* observations were scheduled to avoid contaminating scattered light from all anticipated sources: the bright Earth limb, the Moon, and off-axis stars. Also, observations from LCO and *HST* were strictly simultaneous to guarantee that the ZL measured from the ground is exactly the contribution seen by *HST*. As an additional safeguard, observations were scheduled in three visits, allowing us to look for possible off-axis scattered light with the satellite oriented at different roll angles, to safeguard against unidentified photometric anomalies with the instruments, and to confirm the expected modulation in the ZL with the Earth's orbital position.

3. SUMMARY OF EBL DETECTIONS

The individual measurements that are combined to obtain our detections of the EBL are summarized in Table 1. We summarize our confidence intervals on the detected EBL23 in Table 2 and Figure 1. For comparison with the EBL23 fluxes, we have included in Table 2 the integrated flux from individually photometered sources in the HDF, as measured using the photometry package FOCAS (Jarvis & Tyson 1981; Valdes 1982) and published in Williams et al. (1996). As the values in this table show, the mean EBL23 detections in each bandpass are more than 5 times higher than the integrated flux in HDF galaxies as measured by standard photometry.

To help understand this large difference between the detected EBL and the flux in HDF number counts, we have measured the total flux from resolved galaxies in our WFPC2 images (23 AB mag $< V_{555} < 27.5$ AB mag) using a method that we call “ensemble aperture photometry.”

TABLE 2
EBL RESULTS AND UNCERTAINTIES

Bandpass	Random σ_R (68%)	Systematic σ_S (68%)	Combined σ (68%)	EBL ($\pm 1 \sigma$)
Detected EBL23 (WFPC2 + LCO) ^a				
F300W	2.1	1.5	2.5	4.0 (± 2.5)
F555W	0.6	1.3	1.4	2.7 (± 1.4)
F814W	0.4	0.9	0.0	2.2 (± 1.0)
Minimum EBL (WFPC2) ^a				
F300W	0.19	0.13	0.22	3.2 (± 0.22)
F555W	0.003	0.009	0.01	0.89 (± 0.01)
F814W	0.002	0.007	0.01	0.76 (± 0.01)
Detected EBL23 (FOS + LCO) ^a				
F555W	0.7	2.7	2.8	8.5 (± 5.6)
Flux from Detected Sources in HDF ($m > 23$ AB mag)				
F300W				0.66
F450W				0.51
F606W				0.40
F814W				0.27
Published Number Counts ^b				
F300W ($18 < U_{300} < 23$ AB mag)				0.27 (± 0.05)
F555W ($15 < V_{555} < 23$ AB mag)				0.49 (± 0.10)
F814W ($13 < I_{814} < 23$ AB mag)				0.65 (± 0.13)

NOTE.—All fluxes and errors are given in units of 10^{-9} ergs $\text{s}^{-1} \text{cm}^{-2} \text{sr}^{-1} \text{\AA}^{-1}$.

^a The systematic and statistical errors have been combined assuming a flat or Gaussian probability distribution, respectively, as discussed in Paper I. We equate 1σ combined errors with the 68% confidence interval since the combined errors are nearly Gaussian distributed. Individual sources of error contributing to these totals are summarized in Tables 3 and 4 of Paper I and in Table 1 of Paper II.

^b Estimated errors correspond to uncertainties in the fits to published galaxy counts. The values given correspond to 0.081×10^{-20} , 0.46×10^{-20} , and 1.5×10^{-20} ergs $\text{s}^{-1} \text{cm}^{-2} \text{sr}^{-1} \text{Hz}^{-1}$ and are consistent with those used in Pozzetti et al. 1998.

This method is uniquely suited to both our goal of a very accurate measurement of the *ensemble* flux of all galaxies in our images and to our data set, which has zero-point calibration accurate to $\pm 0.1\%$ over each image and negligible scattered light. This method is described in detail in Paper I and summarized below.

Briefly, we identify the *total* flux from detectable galaxies fainter than $V_{\text{cut}} = 23$ AB mag by simply masking out galaxies with $V < V_{\text{cut}}$ AB mag (and all stars) and averaging the flux of every pixel in the frame. From this, we obtain the mean surface brightness of foregrounds plus *all* extragalactic sources, or the average surface brightness per pixel from “objects + sky.” We then mask out *all detected* objects using standard detection apertures (twice the isophotal area) and calculate the average flux in the remaining pixels. From this, we obtain the mean surface brightness outside of the galaxy masks, or the average surface brightness per pixel from “sky.” The difference between these two measurements is then the ensemble surface brightness of all sources within the area of the masks. This assumes that the sky level is uniform, which is the case to better than 1% accuracy in our images. By varying the bright magnitude cutoff (V_{cut}) we choose for measuring “objects + sky,” we can isolate the flux coming from sources fainter than V_{cut} .

As discussed in Paper I, we find that the recovered flux increases steadily with increasing mask size. For example, roughly 20% of the light from galaxies 4 mag above the detection limit lies at radii $\sqrt{2}r_{\text{iso}} < r < 4r_{\text{iso}}$ (see Fig. 2), beyond the standard-size galaxy apertures ($\sqrt{2}r_{\text{iso}}$) used in

faint galaxy photometry packages, such as SExtractor (Bertin & Arnouts 1996) or FOCAS. Because estimates of the sky level in standard photometry packages come from just beyond the detection apertures, these sky estimates will include some fraction of the galaxies’ light and will doubly compound this error. In addition, because galaxy apertures start to significantly overlap in our images and the HDF images when they extend to $r \sim 4r_{\text{iso}}$, we find that some flux from the wings of *detected* galaxies will inevitably contribute a pedestal level to the mean sky level in any image. We have estimated this pedestal level by Monte Carlo simulations as described in Appendix B of Paper I. The pedestal is independent of field but does depend on the detection limits and surface brightness characteristics of the data. For V_{606} HDF images, this pedestal level is roughly 10% of the total flux from $V > 23$ AB mag galaxies, and again, this error is compounded by the fact that any flux at radii beyond galaxy apertures can be included in the “sky” estimate. The true flux from $V > 23$ AB mag galaxies in the HDF is therefore almost twice what is recovered by standard methods (see § 4.1).

Using different values of V_{cut} , we can quantify systematic errors in faint galaxy photometry as a function of the isophotal surface brightness limit of the data μ_{iso} and the central surface brightness of the source μ_0 . The smaller the value of $\Delta\mu = \mu_{\text{iso}} - \mu_0$ is for a particular galaxy, the larger the photometric error in standard aperture photometry. This problem has been discussed in the literature at length with respect to low surface brightness galaxies at low red-

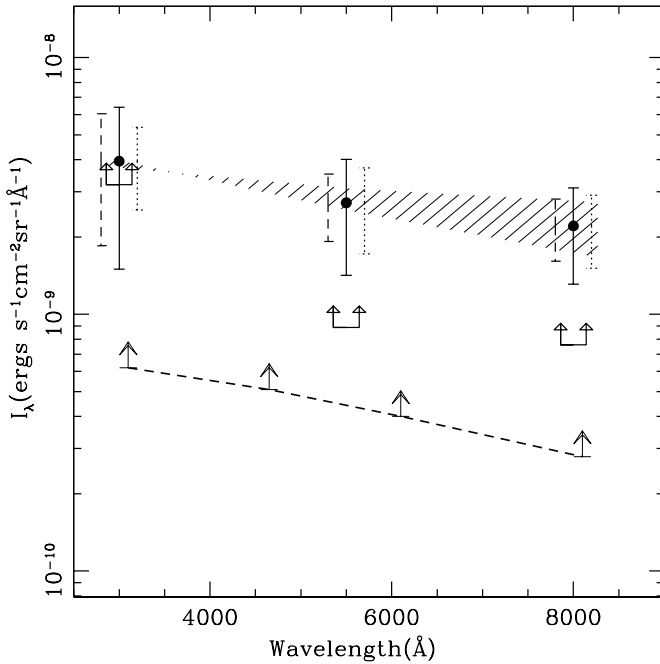


FIG. 1.—Summary of EBL23 measurements, repeated from Paper I. The filled circles show the EBL23 obtained from surface photometry of the total background measured from *HST*/WFPC2, the ZL as measured from LCO, and models of the DGL as summarized in § 3. The solid, dotted, and long-dashed error bars show the combined, systematic, and random 1σ errors, respectively. The hatched region shows the 1σ uncertainty in the detected EBL due to uncertainty in ZL color. The lower-limit arrows connected by a dashed line indicate the total flux from individually photometered galaxies with magnitudes $23 \text{ AB mag} < V_{555} < 30 \text{ AB mag}$ in the HDF catalog. The U-shaped lower-limit arrows show min EBL23, which is the flux as determined by ensemble photometry from galaxies with $23 \text{ AB mag} < V_{555} \leq 28 \text{ AB mag}$ in the EBL fields.

shifts based on extrapolations of simple exponential light profiles (Disney 1976; Disney & Phillips 1983; Davies 1990); the same principle begins to apply to normal surface brightness galaxies that have low *apparent* surface brightness at higher redshifts because of $(1+z)^4$ surface brightness dimming (Dalcanton 1998).

Finally, we note that the direct measurements of the EBL23 in our data—based on surface photometry of the total integrated background, zodiacal light, and diffuse galactic light—are $2\text{--}3\sigma$ detections. However, the mean flux from detected sources is obviously an absolute minimum value for the EBL. Therefore, the strongest lower limit we can place on the flux from sources fainter than $V = 23 \text{ AB mag}$ (EBL23) is the mean flux in *detected* galaxies as measured by ensemble aperture photometry in our WFPC2 data and the HDF. The strongest upper limits we can place on EBL23 are the 2σ upper limits of our direct measurements of the EBL23. In Table 2 we list (1) our direct measurements of the EBL23 and (2) the minimum values for the EBL23 (min EBL23) as identified by ensemble aperture photometry of detected sources in our WFPC2 data and the HDF. For comparison, the flux in published HDF galaxy counts and ground-based counts are also listed there.

4. COMPARISON WITH NUMBER COUNTS AND LUMINOSITY FUNCTIONS

Whether the light originates from stellar nucleosynthesis, accretion onto compact objects, or gravitationally collaps-

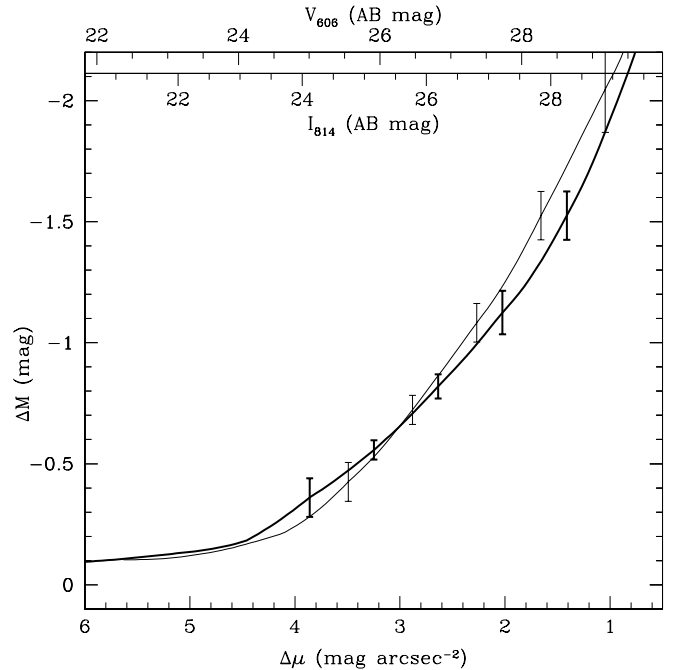


FIG. 2.—Aperture corrections as a function of $\Delta\mu = \mu_{\text{iso}} - \mu_0$ (isophotal minus central surface brightness) derived by “ensemble aperture photometry” of the EBL field for V (heavy line) and I (thin line). The mean apparent magnitude in V_{606} and I_{814} corresponding to a particular value of $\Delta\mu$ in the HDF images is indicated by the x -axes at the top of the plot. Error bars show the 1σ statistical error in the mean corrections derived from 18 WFPC2 images of the EBL field (six exposures, three WF chips).

ing stellar systems, the total optical flux escaping from detected galaxies is quantified by number counts and luminosity functions. To the detection limits, number counts and luminosity functions contain exactly the same information regarding the integrated background light: the integrated flux from resolved sources is the same whether or not you know the redshift of the sources. However, in the context of predicting the EBL flux, luminosity functions contain information about the intrinsic flux distribution of the sources and thus allow us to estimate the flux from sources beyond the detection limits with better defined assumptions. In the following sections, we compare our EBL detections with the integrated flux obtained by both methods. Dust obscuration in the emitting sources will clearly reduce the UV and optical flux that escapes, but the EBL, number counts, and luminosity functions are all measurements of the *escaping* flux; the relative comparisons discussed in this section are therefore independent of dust extinction.

4.1. Number Counts

Using “ensemble aperture photometry” to measure the total flux from galaxies as a function of magnitude in our V_{555} and I_{814} images of the EBL field, we find that the standard photometry methods used to produce the HDF catalog systematically underestimate the flux from each source, as summarized in § 3 (see § 10 and Appendix B of Paper I for a thorough discussion). We use these results to derive flux corrections as a function of $\Delta\mu = \mu_{\text{iso}} - \mu_0$ (isophotal minus central surface brightness), which are essentially aperture corrections. These aperture corrections are similar to those found by other authors (e.g. Smail et al. 1995) and are a natural consequence of integrating an extended light profile to

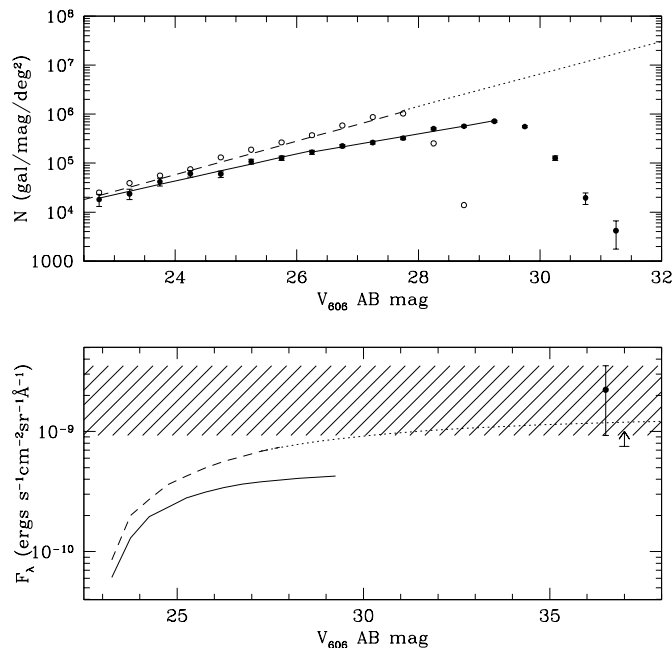


FIG. 3.—*Top*: Galaxy counts as published in the HDF catalog (*filled circles*) with \sqrt{N} error bars and the corrected number counts (*open circles*), as described in § 4.1. The solid lines show fits to the raw number counts, which change slope slightly around $V_{606} = 26$. The fit to the corrected counts is indicated by the dashed line to the detection limit and a dotted line beyond. No change in slope is apparent at the faint end for the corrected counts. All slopes are given in the text. *Bottom*: Integrated flux corresponding to the galaxy counts with the same line types as in the upper panel. The data point and 1σ error bar mark the value of EBL23 (converted to V_{606} from the V_{555} band). The corresponding $\pm 1\sigma$ error range is emphasized by the hatched region. For comparison, the lower-limit arrow shows 2σ lower limit of min EBL23, the integrated flux from detected sources with $V_{606} > 23$ AB mag.

an insufficient radius. This effect can be quantified for exponential or de Vaucouleurs profiles, as in Dalcanton (1998). However, the corrections we show here are empirical measurements and assume nothing about the light profiles of the sources.

The corrections we derive for the two bandpasses (see Fig. 2) are very similar functions of $\Delta\mu$, which indicates that the profiles of detected galaxies are not a strong function of wavelength over the baseline of observed V to I . However, we note that a particular value of $\Delta\mu$ occurs at a brighter AB magnitude in I_{814} than in V_{606} because the limiting isophotal level (sky noise) in I_{814} is 0.6 AB mag brighter than in V_{606} . The corrections are therefore larger in I_{814} than they are at the same AB magnitude at V_{606} . The corrections in both bands include a correction that compensates for overestimates in the sky flux from foreground sources (the pedestal sky level described in § 3). This correction, which accounts for errors in the local sky estimate, ranges from 0.1 to 0.3 mag, monotonically increasing toward fainter magnitudes. As in V_{606} and I_{814} , aperture corrections for the U_{300} band will depend on the profiles of galaxies at U_{300} and the surface brightness limits of the data. However, the very low signal-to-noise ratio of our F300W images prevents us from determining aperture corrections in that bandpass. The U_{300} photometry is discussed further below.

We have applied the aperture corrections we derive to the individual objects in the HDF V_{606} and I_{814} catalogs (Williams et al. 1996), which fractionally increases the flux of each galaxy. For example, while galaxies in the HDF cat-

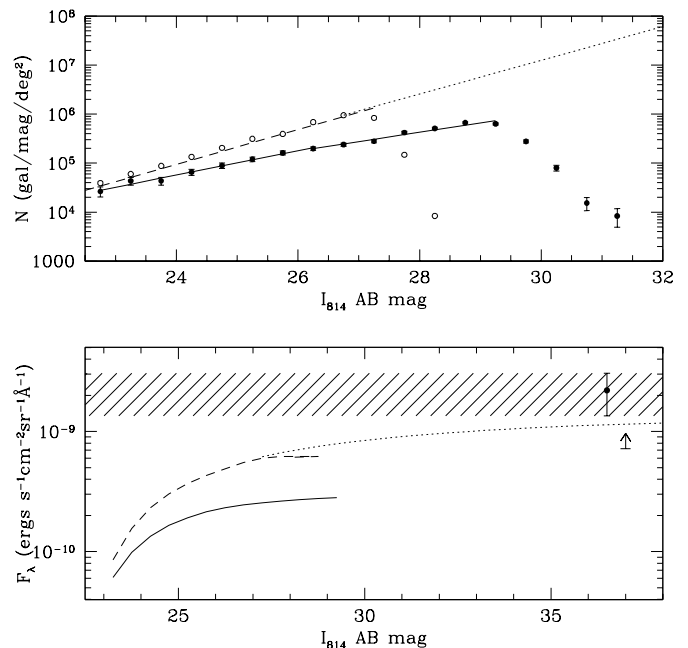


FIG. 4.—Same as Fig. 3, but for the I_{814} band. As for the V_{606} band, the raw I_{814} counts show a slight change in slope around 24–26 AB mag, while the corrected counts do not. All slopes are given in the text. The integrated flux of the raw and corrected counts are compared to our EBL23 I_{814} detections in the lower panel, as in Fig. 3.

alog with $V_{606} \sim 30$ AB mag have well-detected cores, less than 30% of their total flux is recovered: the total flux of a galaxy measured to have $V_{606} \sim 30$ AB mag by standard photometry methods is actually closer to $V_{606} \sim 28$ AB mag. The corrected and uncorrected (raw) galaxy counts and corresponding integrated flux with magnitude are compared in Figures 3 and 4. The integrated flux of the corrected galaxy counts roughly corresponds to the minimum value of EBL23 since the aperture corrections were derived from the calculation of the minimum EBL23 in our data. Statistical variations in galaxy counts between fields are to be expected.

The aperture corrections we apply clearly have a significant impact on the slope of faint number counts. To quantify this, we fit both the raw and corrected number counts with the usual relationship between apparent magnitude and surface number density, $N \propto 10^{\alpha m}$, where N is the number of galaxies per magnitude per square degree. For the raw V_{606} counts, we find that the data exhibit a change in slope around 24–26 AB mag. A single fit over the range $22 \text{ AB mag} < V_{606} < 29.5 \text{ AB mag}$ gives $\alpha = 0.24 \pm 0.01$ with a χ^2 per degree of freedom (χ^2/dof) of 1.5. Fitting the counts brighter and fainter than 26 AB mag, respectively, we find $\alpha_b = 0.28 \pm 0.02$ with $\chi^2/\text{dof} = 0.9$ and $\alpha_f = 0.21 \pm 0.01$ with $\chi^2/\text{dof} = 1.2$ (solid lines in the upper panel of Fig. 3). We ascribe this change in slope to the onset of significant photometry errors.

For the corrected V_{606} counts, we find that the full $22 \text{ AB mag} < V_{606} < 27.5 \text{ AB mag}$ range is well fitted by a slope of $\alpha = 0.33 \pm 0.01$ with $\chi^2/\text{dof} = 0.60$ (dashed line in the upper panel of Fig. 3). This result suggests that photometry errors are responsible for the change in slope at the faint end of the HDF counts and that $N(m)$ does not, in fact, significantly decline before the detection limit of the HDF at V_{606} . In addition, while the integrated flux in the raw galaxy

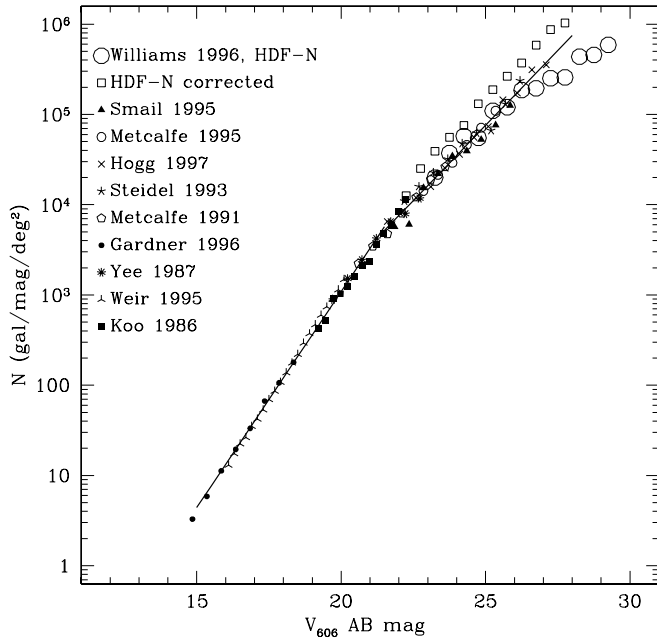


FIG. 5.—Raw and corrected number counts from Fig. 3 compared to number counts from the literature, labeled by first author. The lines indicate fits to the data using the relation $N \propto 10^{\alpha m}$; $\alpha = 0.48 \pm 0.1$ and $\alpha = 0.33 \pm 0.01$ at the bright and faint ends, respectively. Note that the slope of the corrected HDF counts is well matched to that at brighter magnitudes.

counts has converged by the apparent detection limit of the HDF, the flux from the *corrected* galaxy counts has not (see the lower panel of Fig. 3).

We find similar results for the I_{814} counts (see Fig. 4). As for V_{606} , the raw I_{814} counts display a slight change in slope around 24–26 AB mag. We find a slope of $\alpha_b = 0.25 \pm 0.01$ with $\chi^2/\text{dof} = 0.6$ and $\alpha_f = 0.19 \pm 0.02$ with $\chi^2/\text{dof} = 2.0$, brighter and fainter than 26 AB mag, respectively. For the full range $22 \text{ AB mag} < I_{814} < 29.5 \text{ AB mag}$, we find $\alpha = 0.22 \pm 0.01$ with $\chi^2/\text{dof} = 2.1$. For the corrected I_{814} counts, we find $\alpha = 0.34 \pm 0.01$ with $\chi^2/\text{dof} = 0.8$ at $22 \text{ AB mag} < I_{814} < 27 \text{ AB mag}$.

In Figure 5 we show the raw and corrected HDF counts relative to V - and R -band counts available in the literature for $V > 15 \text{ AB mag}$ (Data in Figs. 5 and 6 come from Williams et al. 1996, Smail et al. 1995, Metcalfe et al. 1991, 1995; Hogg et al. 1997; Steidel & Hamilton 1993; Gardner et al. 1996; Yee & Green 1987; Weir, Djorgouski, & Fayyad 1995, Koo 1986; Lilly, Cowie, & Gardner 1991; Tyson 1988; and Hall & Makay 1984.) We have converted all of the published counts to V -band AB magnitudes by applying constant offsets consistent with those in Fukugita, Shimasaku, & Ichikawa (1995). These incorporate mean K -corrections based on the mean redshift corresponding to the apparent magnitude of the sample. Differences between filters will have some effect on the slope of counts in surveys that cover a large range of redshift (apparent magnitude) due to changing galaxy colors and K -corrections with increasing redshift, but these effects will average out between the multiple surveys shown. This plot shows that the aperture corrections we have applied to the HDF sources produce number counts that have a slope consistent with the slope found at brighter magnitudes.

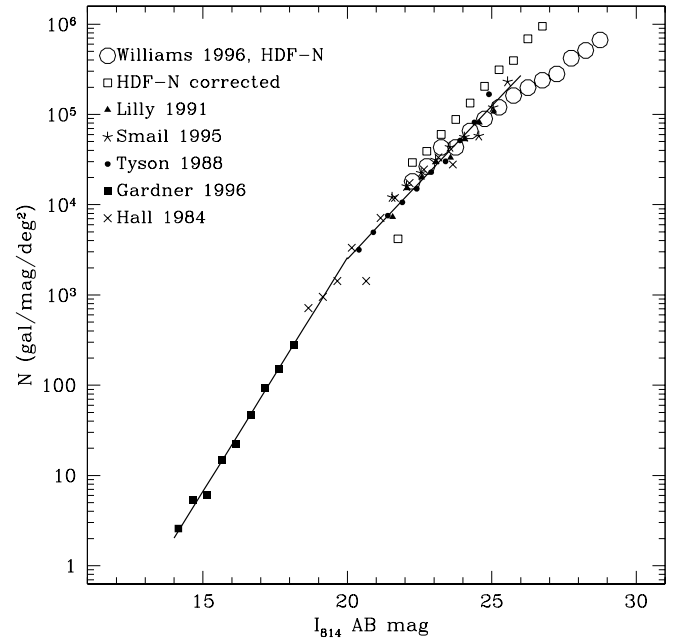


FIG. 6.—Same as Fig. 5, but for the I -band counts. The lines indicate fits to the data using the relation $N \propto 10^{\alpha m}$; $\alpha = 0.52 \pm 0.1$ and $\alpha = 0.34 \pm 0.01$ at the bright and faint ends, respectively. Note that slope of the corrected HDF counts is well matched to the slope at brighter magnitudes and that the slope of the I - and V -band counts are similar at all magnitudes.

In Figure 6 we show the same plot for the I band. Again, the corrected I_{814} counts display a slope that is similar to that found at magnitudes brighter than 23 AB mag. Note also that slope of the counts at less than 25 AB mag in V and I are the same to within the statistical errors. The aperture corrections we apply to the HDF counts at V_{606} and I_{814} extend this agreement to the current detection limits. The corrected counts imply that the faintest galaxies detected do not exhibit a significantly steeper slope in V_{606} than in I_{814} , in contrast to the raw galaxy counts. This is an important constraint on galaxy evolution models.

Although the signal-to-noise ratio in the U_{300} data is too low to allow us to obtain accurate aperture corrections at that wavelength, the minimum EBL23 at U_{300} implies consistent colors for faint and bright galaxies at $U-V$, as in $V-I$ (see Fig. 1 and Table 2). We note, also, that the color of the integrated flux from galaxies is consistent with the color of the total background light within 2σ . In other words, no exotic population of sources is required to produce the detected background.

The lack of turnover in the corrected counts strongly suggests that sources do exist at apparent magnitudes beyond the present detection limit. If we impose no limit on the apparent magnitude of sources and simply extrapolate the galaxy counts beyond $V_{606} \sim 27.5 \text{ AB mag}$ using $\alpha = 0.33$ (dotted line in Fig. 3), we obtain a prediction for the total integrated EBL23 of $1.3 \times 10^{-9} \text{ cgs}$, which is 1σ below the measured value in the EBL field. In this case, the predicted EBL23 converges around $V_{606} \sim 50 \text{ AB mag}$, which is significantly fainter than a dwarf galaxy at $z \sim 6$. However, very little flux is obtained from the faintest bins. If we impose the limit $V_{606} \sim 38 \text{ AB mag}$ as the faintest apparent magnitude for a realistic source (e.g., a dwarf galaxy with $M_V \sim -10 \text{ AB mag}$ at $z \sim 4$), we obtain a flux of 1.2×10^{-9}

cgs. The flux from sources with $I_{814} > 23$ AB mag is 1.3×10^{-9} cgs if we adopt $\alpha = 0.34$, with the flux converging around $I_{814} \sim 60$ AB mag. Adopting a more realistic faint cutoff of ~ 38 AB mag, as discussed for V_{606} , we obtain a total flux of 1.2×10^{-9} cgs, 1σ below the mean detected value of EBL23 at I_{814} (see Fig. 4).

In order to obtain a cumulative flux equal to the mean detected EBL (or the upper limit) from sources brighter than ~ 38 mag, the slope of the galaxy counts in the range 28–38 AB mag would clearly need to *increase* at some point beyond the current detection limit. For example, the total flux from sources 23 AB mag $< V_{606} < 38$ AB mag will produce the mean detected EBL if the sources with 23 AB mag $< V_{606} < 28$ AB mag obey a slope of $\alpha = 0.33$ and sources with 28 AB mag $< V_{606} < 38$ AB mag obey $\alpha = 0.42$. We stress, however, that the total flux obtained from sources with such a steep faint-end slope is critically dependent on the cut of magnitude: the total flux reaches 5.1×10^{-9} cgs if we integrate the counts to 50 AB mag and 9.0×10^{-9} cgs if we integrate to 60 AB mag. Recall that our 2σ upper limit on EBL23 at V_{606} is 5.0×10^{-9} cgs. For $\alpha = 0.35$ at $V > 28$ AB mag, the integrated flux reaches 1.37, 1.51, and 1.57×10^{-9} cgs (converged) for faint cutoff magnitudes of 40, 60, and 80 AB mag, respectively. Although it is obviously impossible to place firm constraints on the number counts beyond the detection limit since they may change slope at any magnitude, we conclude that it is very unlikely that the slope beyond $V_{606} \sim 28$ AB mag is steeper than $\alpha = 0.42$. If the slope continues at $0.33 < \alpha < 0.35$, the EBL23 reaches roughly $(1.3\text{--}1.5) \times 10^{-9}$ cgs by $V_{606} \sim 40$ AB mag, less than 1σ below our detected value.

Similarly, for the I band the integrated flux from sources matches the mean detected EBL23 if the sources with 23 AB mag $< I_{814} < 27$ AB mag obey a slope of $\alpha = 0.34$ and sources with 27 AB mag $< I_{814} < 39$ AB mag obey $\alpha = 0.42$. For those slopes, the total flux reaches the 2σ upper limit of the EBL23 at I_{814} by 50 AB mag. For $\alpha = 0.36$, slightly above the slope we find for the corrected counts, the integrated flux reaches 1.31×10^{-9} , 1.58×10^{-9} , and 1.62×10^{-9} cgs (converged) for faint cutoff magnitudes of 40, 60, and 80 AB mag, respectively. As for the V band, we conclude that it is unlikely that the I -band faint-end slope is steeper than 0.42 at any magnitude. For a slope of $0.34 < \alpha < 0.36$ for $I > 27$ AB mag, the EBL reaches $(1.2\text{--}1.3) \times 10^{-9}$ by $I_{814} \sim 40$ AB mag, 1σ below our detected value.

In summary, we conclude from the corrected number counts shown in Figures 3–6 that sources are likely to exist beyond the detection limit of the HDF. Furthermore, if the number counts continue with the slope we measure at the faintest levels, then the predicted EBL23 is within 1σ of the detected EBL23 at both V_{606} and I_{814} . If we extrapolate beyond the detection limits assuming the slope found from the corrected number counts, we find that less than 50% of EBL23 comes from sources beyond the current detection limit at V_{606} or I_{814} —the majority of the light contributing to EBL23 comes from sources that can be individually detected.

Finally, we note that our ensemble photometry method yields a statistical correction for the light lost from the wings of galaxies beyond the detection isophote. This light cannot, by definition, be recovered by standard single-object photometry. In contrast, the ensemble photometry method

effectively adds together the light beyond the detection isophote from many galaxies to enable a significant measurement of that light.

4.2. Luminosity Functions

In this section we compare the detected EBL with the EBL predicted by luminosity functions measured as a function of redshift. To avoid unnecessary complications in defining apparent magnitude cutoffs and to facilitate comparison with other models of the luminosity density as a function of redshift, we compare luminosity functions with the total EBL rather than with EBL23, as in the previous section. To do so, we combine the EBL23 flux measured in Paper I with the flux from number counts at brighter magnitudes, as given in Table 2. Systematic errors in photometry of the sort discussed in § 4.1 are likely to be relatively small for redshift surveys because the objects selected for spectroscopic surveys are much brighter than the limits of the photometric catalogs (although, see Dalcanton 1998 for discussion of the effects of small, systematic photometry errors on inferred luminosity functions). We have not tried to compensate for such effects here.

The integrated flux from galaxies at all redshifts is given by

$$I(\lambda, 0) = \int_0^z \mathcal{L}(\lambda_z, z) \frac{dV_c(z)}{4\pi D_L(z)^2}, \quad (1)$$

in which $V_c(z)$ is the comoving volume element, $D_L(z)$ is the luminosity distance, λ_0 is the observed wavelength, and $\lambda_z = \lambda_0(1+z)^{-1}$ is the rest-frame wavelength at the redshift of emission. To compare the detected EBL to the observed luminosity density with redshift $\mathcal{L}(\lambda, z)$, we begin by constructing the SED of the *local* luminosity density as a linear combination of SEDs for E/S0, Sb, and Ir galaxies, weighted by their fractional contribution to the local B -band luminosity density:

$$\mathcal{L}(\lambda, 0) = \sum_i \mathcal{L}_i(B, 0) \frac{f_i(\lambda)}{f_i(B)}, \quad (2)$$

in which the subscript i denotes the galaxy Hubble type (E/S0, Sb, or Ir), $f_i(\lambda)$ denotes the galaxy SED (the flux per unit rest-frame wavelength), and $\mathcal{L}_i(B, 0)$ is the B -band, local luminosity density in units of $\text{ergs s}^{-1} \text{Å}^{-1} \text{Mpc}^{-3}$. To produce the integrated spectrum of the local galaxy population, we use Hubble-type-dependent luminosity functions from Marzke et al. (1998) and SEDs for E, Sab, and Sc galaxies from Poggianti (1997). We adopt a local luminosity density of $\mathcal{L}_B = 1.3 \times 10^8 h L_\odot \text{Mpc}^{-3}$, consistent with the Loveday et al. (1992) value adopted by the Canda-France Redshift Survey (CFRS; Lilly et al. 1996) and also with Marzke et al. (1998).⁵ The spectrum we obtain for $\mathcal{L}(\lambda, 0)$ is shown in Figure 7.

We note that the recent measurement of the local luminosity function by Blanton et al. (2001) indicates a factor of 2 higher local luminosity density than found by previous authors. Previous results are generally consistent with Loveday et al. to within 40%. Blanton et al. attribute this increase to deeper photometry that recovers more flux from the low

⁵ For a B -band solar irradiance of $L_\odot = 4.8 \times 10^{29} \text{ ergs s}^{-1} \text{Å}^{-1}$, $\mathcal{L}(B, 0) = 6.1 \times 10^{37} h \text{ ergs s}^{-1} \text{Mpc}^{-3} = 4.0 \times 10^{19} h_{50} \text{ W Hz}^{-1} \text{Mpc}^{-3}$.

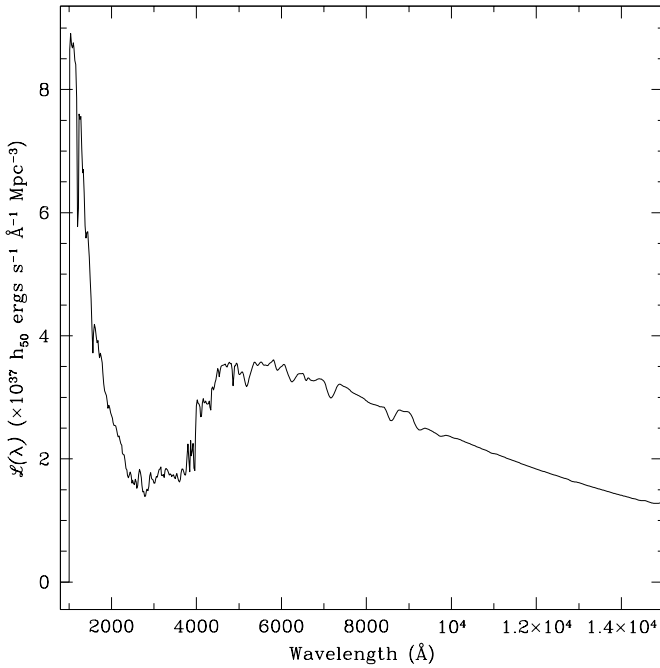


FIG. 7.—Local luminosity density constructed by combining the spectral energy distributions of E/S0, Sab, and Sc galaxies weighted according to the type-dependent luminosity functions as described in § 4.2 and eq. (2).

surface brightness wings of galaxies in their sample relative to previous surveys (see discussions in § 4.1) and photometry that is unbiased as a function of redshift. For the no-evolution and passive-evolution models discussed below, the implications of the Blanton et al. results can be estimated by simply scaling the resulting EBL by the increase in the local luminosity density. Although the Blanton et al. results do not directly pertain to the luminosity functions measured by CFRS at redshifts $z > 0.2$, they do suggest that redshift surveys at high redshifts will underestimate the luminosity density, as discussed by Dalcanton (1998).

In the upper panel of Figure 8, we compare the EBL flux we detect with the EBL flux predicted by five different models for $\mathcal{L}(\lambda, z)$, using the local luminosity density derived in equation (2) as a starting point. For illustrative purposes, the first model we plot shows the EBL that results if we assume no evolution in the luminosity density with redshift, i.e., $\mathcal{L}(\lambda, z) = \mathcal{L}(\lambda, 0)$. The number counts themselves rule out a nonevolving luminosity density, as has been discussed in the literature for over a decade; inconsistency between the detected EBL and the no-evolution model is just as pronounced. The predicted EBL for the no-evolution model is a factor of 10 fainter than the detected values (*filled circles*). These are 1.7, 2.1, and 2.2 σ discrepancies at U_{300} , V_{555} , and I_{814} , respectively. More concretely, the no-evolution prediction is at least a factor of 12, 4, and 3.7 times lower than the flux in *individually resolved* sources at U_{300} , V_{555} , and I_{814} , respectively (*lower-limit arrows*). Note that the no-evolution model still underpredicts the EBL if we rescale the local luminosity density to the Blanton et al. (2001) values. This model demonstrates the well-known fact that luminosity density is larger at higher redshifts.

The second model we plot in Figure 8 shows the effect of passive evolution on the color of the predicted EBL. In this model, we have used the Poggianti (1997) SEDs for galaxies as a function of age for $H_0 = 50 \text{ km s}^{-1}$

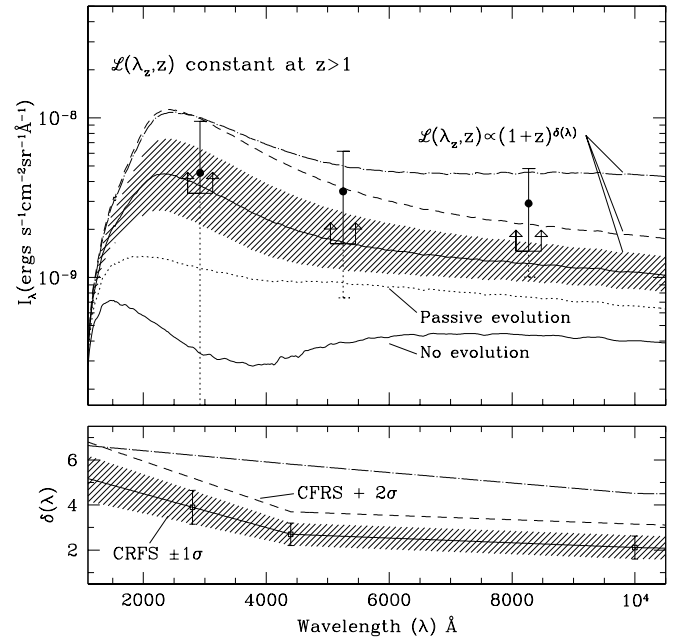


FIG. 8.—*Top*: Spectrum of the EBL calculated by integrating the luminosity density over redshift (eq. [1]) for constant luminosity density, passively evolving luminosity density, and evolution of the form $\mathcal{L}(\lambda, z) = \mathcal{L}(\lambda, 0)(1+z)^{\delta(\lambda)}$, with $\mathcal{L}(\lambda, z)$ constant at $z > 1$. *Bottom*: Values of $\delta(\lambda)$ for the three cases of $(1+z)^{\delta(\lambda)}$ as labeled in the figure and described in the text. Line types and hatched regions in upper panel correspond to values of $\delta(\lambda)$ with the same line type in the lower panel. The filled circles show the mean EBL detections with 2σ error bars. The error bars are dashed where they extend below the cumulative flux in detected sources—the minimum values for the EBL—indicated by the lower-limit brackets.

Mpc^{-1} and $q_0 = 0.225$. In the Poggianti models, stellar populations are 2.2 Gyr old at a $z \sim 3$. The resulting $\mathcal{L}(\lambda, z)$ is bluer than the no-evolution model because of a combination of K -corrections and increased UV flux for younger stellar populations. The passive-evolution model does provide a better qualitative match to the SED of the resolved sources (*lower limits*) and EBL detections (*filled circles*); however, it is still a factor of 3 times less than the flux at U_{300} and a factor of 2 times less than the flux we recover from resolved sources at V_{555} and I_{814} . For the adopted local luminosity density and Poggianti models, passive evolution is therefore not sufficient to produce the detected EBL. Again, the passive evolution adopted here still underpredicts the EBL if we rescale the local luminosity density by a factor of 2 to agree with the Blanton et al. (2001) value.

As a fiducial model of evolving luminosity density, we adopt the form of evolution implied by the CFRS (Lilly et al. 1996) and Lyman limit surveys of Steidel et al. (1999): $\mathcal{L}(\lambda, z) = \mathcal{L}(\lambda, 0)(1+z)^{\delta(\lambda)}$ over the range $0 < z < 1$ and roughly constant luminosity density at $1 < z < 4$. The remaining three models shown in Figure 8 test the strength of evolution of that form that is allowed by the EBL detections. The hatched region shows the EBL predicted for values of $\delta(\lambda)$ that represent the $\pm 1\sigma$ range found by CFRS for the redshift range $0 < z < 1$. The value of the exponent $\delta(\lambda)$ is indicated in the lower panel of Figure 8, and the hatched region reflects the uncertainty in the high redshift luminosity density due to the poorly constrained faint-end slope of the luminosity functions. This $\pm 1\sigma$ range of the predicted EBL

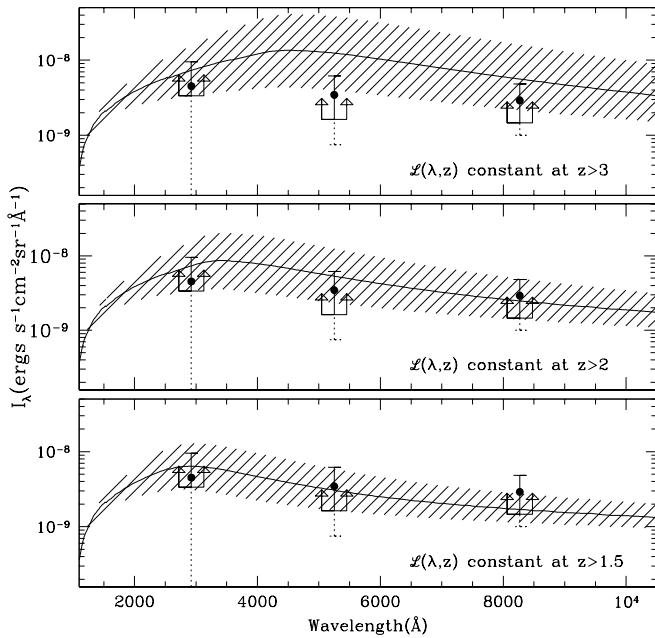


FIG. 9.—Spectrum of the EBL calculated assuming $\mathcal{L}(\lambda, z) = \mathcal{L}(\lambda, 0)(1+z)^{\delta(\lambda)}$ over the range $0 < z < 1.5$ (bottom), $0 < z < 2$ (middle), and $0 < z < 3$ (top). In all cases, the luminosity density is held constant beyond the indicated redshift limit. The hatched regions each show the $\pm 1 \sigma$ range of CFRS values for $\delta(\lambda)$, as in Fig. 8. The integrated EBL as a function of redshift is shown in Fig. 10. Luminosity density as a function of redshift is shown in Fig. 11 for some combinations of $\delta(\lambda)$ and the redshift cutoff for evolution. The filled circles, error bars, and lower-limit symbols are as in Fig. 8.

is consistent with the detected EBL at U_{300} but is inconsistent with the EBL detections at V_{555} and I_{814} at the 1σ level of both model and detections. It is, however, consistent with the integrated flux in detected sources at V_{555} and I_{814} .

To test the range of evolution allowed by the full $\pm 2 \sigma$ range of the EBL detections, we can explore two possibilities: (1) stronger evolution at $0 < z < 1$, shown in Figure 8, and (2) evolution continuing beyond $z = 1$, shown in Figures 9, 10, and 11. Addressing the possibility of constant luminosity density at $z > 1$, the dashed line in the upper panel of Figure 8 shows the EBL predicted by the 2σ upper limit for $\delta(\lambda)$ from CFRS; the dot-dashed line corresponds to the value of $\delta(\lambda)$ required to obtain the upper limits of the EBL detections at all wavelengths. Note that the latter implies a value for $\mathcal{L}(4400 \text{ \AA}, 1)$, which is ~ 10 times higher than the value estimated by CFRS. This result emphasizes that the 2σ interval of the EBL detections spans a factor of 4 in flux at 4400 \AA , and thus the allowed range in the luminosity density for $\lambda < 4400 \text{ \AA}$ and $0 < z < 1$ is similarly large. Also, for each model in which the luminosity density is constant at $z > 1$, less than 50% of the EBL will come from beyond $z = 1$ because of the combined effects of K -corrections and the decreasing volume element with increasing redshift (see Fig. 10).

Evolution continuing beyond $z = 1$ is possible if the Lyman limit-selected surveys have not identified all of the star formation at high redshifts and estimates of the luminosity density at $3 \lesssim z \lesssim 4$ are subsequently low. Figures 9 and 10 show the EBL predicted by models in which the luminosity density increases as $(1+z)^{\delta(\lambda)}$ to redshifts of $z = 1.5, 2$ and 3 . Clearly, significant flux can come from $z > 1$ if the luminosity density continues to

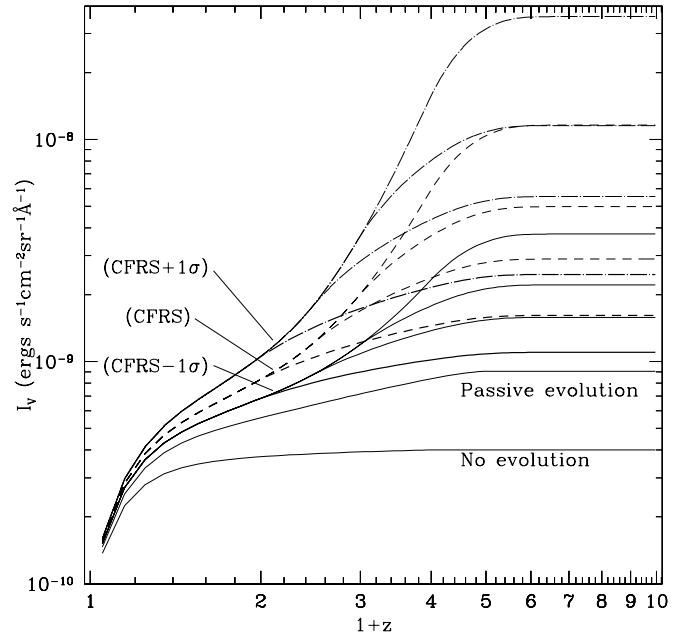


FIG. 10.—Integrated EBL at V_{555} contributed as a function of increasing redshift from $z = 0$ to $z = 10$. As marked in the figure, the lines show the integrated flux for no evolution in the luminosity density, passive evolution and evolution of the form $\mathcal{L}(\lambda, z) \propto (1+z)^{\delta(\lambda)}$ for the -1σ , mean, and 1σ range of $\delta(\lambda)$ values determined by CFRS. For each $\delta(\lambda)$, we plot the growth of the EBL with redshift if $\mathcal{L}(\lambda, z)$ is held constant at $z > 1, z > 1.5, z > 2$, and $z > 3$, corresponding to Figs. 8 and 9.

increase as a power law. The rest-frame U_{300} luminosity density is plotted as a function of redshift in Figure 11 for limiting values of the cutoff redshift for evolution and $\delta(\lambda)$. Although the strongest evolution plotted overpre-

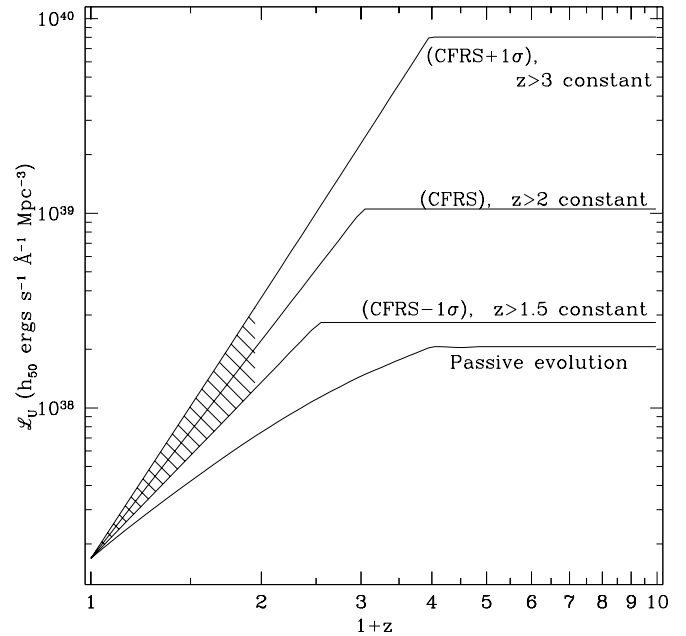


FIG. 11.—Luminosity density at U_{300} as a function of redshift corresponding to limiting cases plotted in Fig. 9. The hatched region indicates the $\pm 1 \sigma$ range given by the CFRS measurements of $\delta(\lambda)$ over the range $0 < z < 1$. The horizontal line segments show the luminosity density corresponding to the -1σ limit for $\delta(\lambda)$ held constant at $z > 1.5$, the mean value for $\delta(\lambda)$ held constant at $z > 2$, and the 1σ limit for $\delta(\lambda)$ held constant at $z > 3$.

dicts the detected EBL, our detections are clearly consistent with some of the intermediate values of the $\delta(\lambda)$ and increasing luminosity density beyond $z = 1$. For example, the mean rate of increase in the luminosity density found by CFRS can continue to redshifts of roughly 2.5–3 without overpredicting the EBL.

In all models, we have adopted the same cosmology ($h = 0.5$ and $\Omega = 1.0$) as assumed by CFRS and Steidel et al. (1999) in calculating $\mathcal{L}(\lambda, z)$ and $\delta(\lambda)$. Although the luminosity density inferred from these redshift surveys depends on the adopted cosmological model, the flux per redshift interval is a directly observed quantity. The EBL is therefore a directly observed quantity over the redshift range of the surveys and is also model-independent. To the degree that the luminosity density becomes unconstrained by observations at higher redshifts, the EBL does depend on the assumed (not measured) luminosity density and on the adopted cosmology through the volume integral. Although dependence of the predicted EBL on H_0 cancels out between the luminosity density, volume element, and distance in equation (1), H_0 has some impact through cosmology-dependent timescales, which affect the evolution of stellar populations. If the luminosity density is assumed to be constant for $z > 1$, the predicted EBL increases by 25% at V_{555} for ($\Omega_M = 0.2, \Omega_\Lambda = 0$) and corresponding values of $\delta(\lambda)$ and decreases by 50% for (0.2, 0.8). The luminosity densities corresponding to the 2σ upper limit of the detected EBL change by the same fractions for the different cosmologies if \mathcal{L} is constant at $z > 1$. Similarly, for models in which the luminosity density continues to grow at $z > 1$, the luminosity density required to produce the EBL will be smaller if we adopt (0.2, 0) than (1, 0) and smaller still for (0.2, 0.8). The exact ratios depend on the rate of increase in the luminosity density.

Several authors (Treyer et al. 1998; Cowie, Songaila, & Barger 1999; Sullivan et al. 2000) have found that the \mathcal{L} at UV wavelengths (2000–2500 Å) is higher than claimed by CFRS (2800 Å) in the range $0 < z < 0.5$ and have found weaker evolution in the UV luminosity density, corresponding to $\delta(2000 \text{ Å}) \sim 1.7$. The implications for the predicted EBL can be estimated from the plots of the $\mathcal{L}(U_{300}, z)$ shown in Figure 11 and the corresponding EBL in Figures 9 and 10. For instance, if the local UV luminosity density is a factor of 5 higher than the value we have adopted and if $\delta(2000 \text{ Å}) \sim 1.7$ over the range $0 < z < 1$, then the rest-frame UV luminosity density at $z = 1$ is similar to that measured by CFRS, and the predicted U_{300} EBL will be roughly 3.5×10^{-9} cgs, very similar to the EBL we derive from our modeled local luminosity density and the mean values for $\delta(\lambda)$ from CFRS.

4.3. Discussion

Evolution in the luminosity density of the form $(1+z)^{\delta(\lambda)}$ at $0 < z < 1$ and slower growth or stabilization at $z > 1$, such as suggested by redshift surveys at $0 < z < 4$, is consistent with the detected EBL for values of $\delta(\lambda)$ consistent with CFRS. The strongest constraints we can place on the EBL span a factor of 5 in flux. As such, stronger evolution between $0 < z < 1$ than reported by CFRS or continuing evolution at $z > 1$ cannot be tightly constrained. We note that recent results from Wright (2000), which constrain the 1.25 μm EBL flux to be $2.1(\pm 1.1) \times 10^{-9}$ cgs, are in good agreement with our results but do not improve the con-

straints on the high-redshift optical luminosity density over those discussed above.

In contrast to our results, previous authors have claimed good agreement between the flux in the raw number counts from the HDF and integrated flux in the measured CFRS luminosity density to $z = 1$ under the assumption that the luminosity density *drops rapidly* at $z > 1$ (Madau, Pozzetti, & Dickinson 1998; Pozzetti et al. 1998). In those comparisons the errors in faint galaxy photometry that cause $\sim 50\%$ underestimates of the total light from $V > 23$ galaxies (discussed in § 4.1) are compensated by the assumption that the luminosity density drops rapidly beyond $z = 1$. That assumption was based on measurements of the flux from Lyman limit systems in the HDF field by Madau et al. (1996), which are substantially lower than measurements by Steidel et al. (1999) because of underestimates of the volume corrections and the small-area sampling. We find that the detected EBL is *not* consistent with luminosity evolution comparable to the CFRS-measured values at $0 < z < 1$ if the luminosity density drops rapidly at $z > 1$.

5. FLUX FROM SOURCES BELOW THE SURFACE BRIGHTNESS DETECTION LIMIT

The fractional EBL23 flux that comes from *detected* sources is simply the ratio of the flux in detected sources (measured by “ensemble photometry”) to the detected EBL23 ($\pm 2\sigma$ limits). The maximum fractional EBL23 flux coming from *undetected* sources is what remains: 0%–65% at U_{300} , 0%–80% at V_{555} , and 0%–80% at I_{814} . Although these limits include the possibility of no additional contribution from undetected sources, it is worthwhile to note that if the progenitor of a normal disk galaxy at $z = 0.1$ [central surface brightness $\mu_0(V) \sim 21.3$ mag arcsec $^{-2}$ and $V \sim 22$ mag] existed at $z \sim 2$, then the $z \sim 2$ progenitor would have a core surface brightness (within 0.2×0.2 arcsec 2) of ~ 26 mag arcsec $^{-2}$ for standard K -corrections and passively evolving stellar populations (see, e.g., Poggianti 1997), which is roughly the detection limit for the HDF. In particular, regardless of the exact evolutionary or K -corrections, dimming due to cosmological effects alone (redshift and angular resolution) produces ~ 5 mag of surface brightness dimming. This effect is independent of wavelength, so that dimming at other bandpasses is similar, modulo differences in the evolutionary and K -corrections (shown in Figs. 12, 13, and 14). At I , for example, the drop in surface brightness for a disk galaxy at $z \sim 2$ relative to $z \sim 0$ is ~ 0.5 mag greater than for V . The progenitor of a typical disk galaxy at $z = 0.1$, which has $V-I \sim 0.9$ and $\mu_0(I) \sim 20.3$ mag arcsec $^{-2}$ (de Jong & Lacey 2000), will have $V-I \sim 0.5$ at $z \sim 2$ and $\mu_0(I) \sim 25.5$. Thus, the typical disk galaxy at $z \sim 2$ is close to the HDF detection limit in I as well as V . Irrespective of the color evolution with redshift, the point is that cosmological surface brightness dimming alone suggests that a significant fraction of the EBL23 may come from normal galaxies at redshifts $z < 4$, which are undetectable in the HDF. Furthermore, recent redshift surveys for low surface brightness (LSB) galaxies now suggest that the distribution of galaxies in μ_0 is nearly flat for $\mu_0 > 22.0B$ mag arcsec $^{-2}$ at some luminosities (Sprayberry et al. 1997; Dalcanton et al. 1997; O’Neil & Bothun 2000; Blanton et al. 2001; Cross et al. 2001). If such populations exist at high redshift, they may contribute significant flux to the EBL as presently undetectable sources.

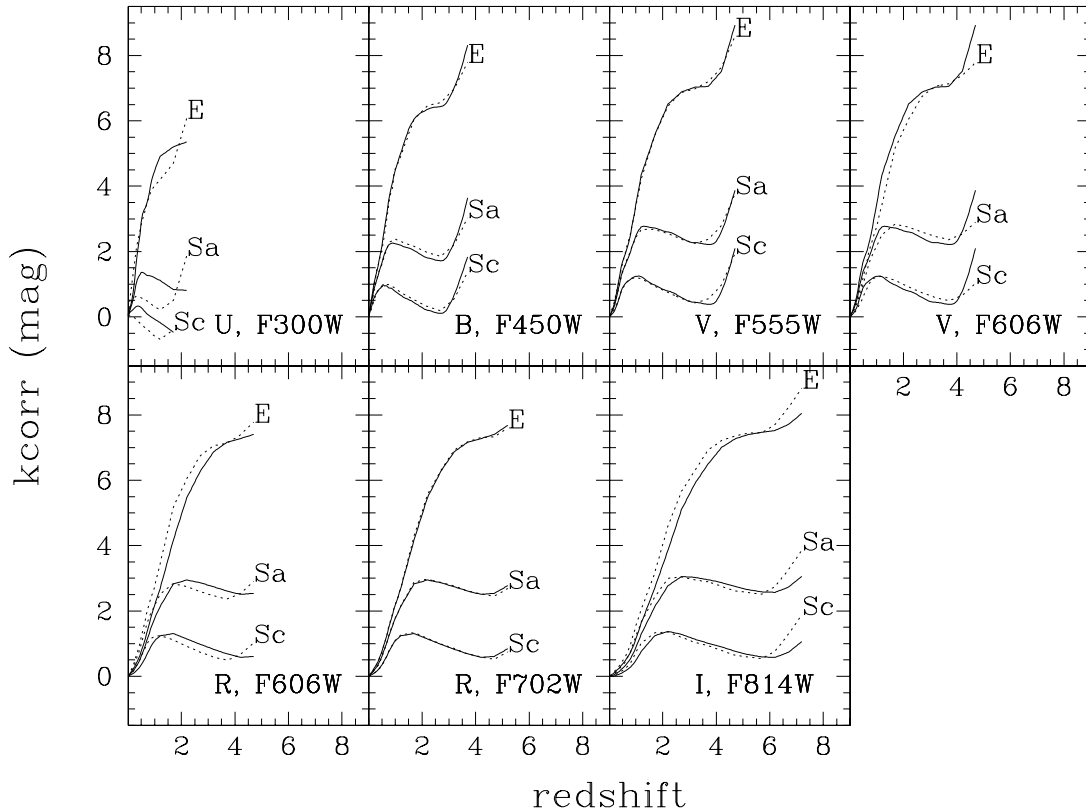


FIG. 12.— K -corrections for various filters as a function of redshift calculated using Poggianti (1997) SEDs for present-day E, Sa, and Sc galaxies. Band-passes are standard Johnson/Cousins filters and the corresponding WFPC2 filters, shown with solid and dotted lines, respectively.

In this section we explore the possible contributions to the EBL23 from galaxies at all redshifts that escape detection in the HDF because of low *apparent* surface brightness. To do so, we have simulated galaxy populations at redshifts $0 < z < 10$ as the passively evolving counterparts of local galaxy populations and then “observed” the simulated galaxies through the Gaussian $0''.1$ FWHM point-spread function of WFPC2. We define the surface brightness detection threshold to be consistent with the 5σ detection limits of the HDF images (see Table 3), which correspond to roughly the turnover magnitude in the number counts. This exercise is not meant to approximate realistic galaxy populations at high redshift; the evolution of galaxy populations in surface brightness, luminosity, and number density is so poorly constrained at present that more specific modeling is unwarranted. The models discussed here simply address the following question: how much of the total flux from a local-type galaxy population at a redshift z can be resolved into individual sources?

5.1. Models

We have considered three models for the central surface brightness distributions of disk galaxies in order to explore the possible contributions from LSB galaxies. These models are taken from Ferguson & McGaugh (1995) and can be generally described as follows: a standard passive-evolution model in which all galaxies have central surface brightnesses in the range $21 \text{ mag arcsec}^{-2} < \mu_0(B_J) < 22 \text{ mag arcsec}^{-2}$ (model PE); an LSB-rich model (model A), in which galaxies of all luminosities have $21.5 \text{ mag arcsec}^{-2} < \mu_0(B_J) < 25 \text{ mag arcsec}^{-2}$; and a more conservative LSB model (model B), in which μ_0 is monotonically decreasing for galaxies fainter than $L/L^* < 1$ and $21 \text{ mag arcsec}^{-2} < \mu_0(B_J) < 22 \text{ mag arcsec}^{-2}$ otherwise (see Fig. 15). We include passive luminosity evolution in all three models since the no-evolution models have been clearly ruled out by both number counts and our own EBL results. Since model A (model PE) has a broader (narrower) surface brightness distribution than is found by recent LSB surveys (Spray-

TABLE 3
ADOPTED DETECTION LIMITS OF THE HDF

<i>HST</i> /WFPC2 Filter	μ_{core} (AB mag arcsec $^{-2}$)	m (AB mag)	Johnson/Cousins Filter	μ_{core} (mag arcsec $^{-2}$)	m (mag)
F300W	25.0	27.5	<i>U</i>	23.9	26.4
F450W	25.8	28.3	<i>B</i>	25.8	28.3
F606W	26.3	28.8	<i>V</i>	25.9	28.4
F606W	26.3	28.8	<i>R</i>	25.5	28.0
F814W	25.8	28.3	<i>I</i>	25.2	27.7

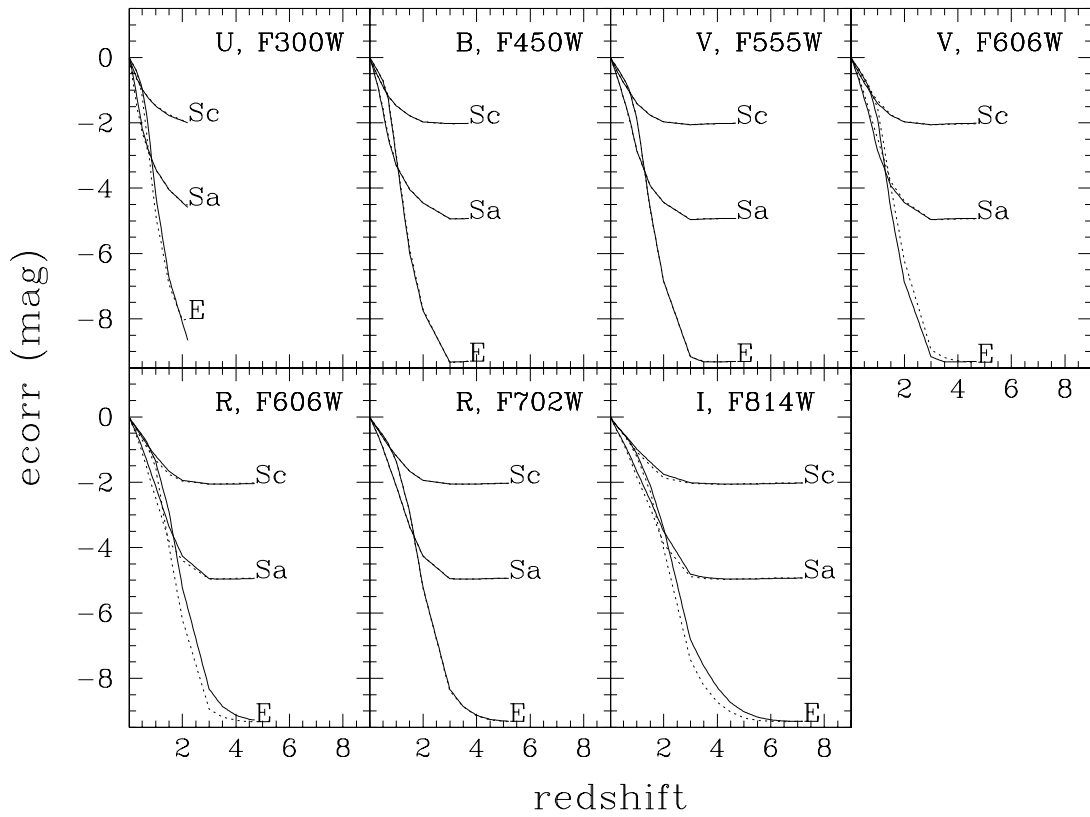


FIG. 13.—Evolutionary corrections for various filters as a function of redshift calculated using Poggianti (1997) SEDs for E, Sa, and Sc galaxies evolving passively with redshift. Bandpasses are standard Johnson/Cousins filters and the corresponding WFPC2 filters, shown with solid and dotted lines, respectively.

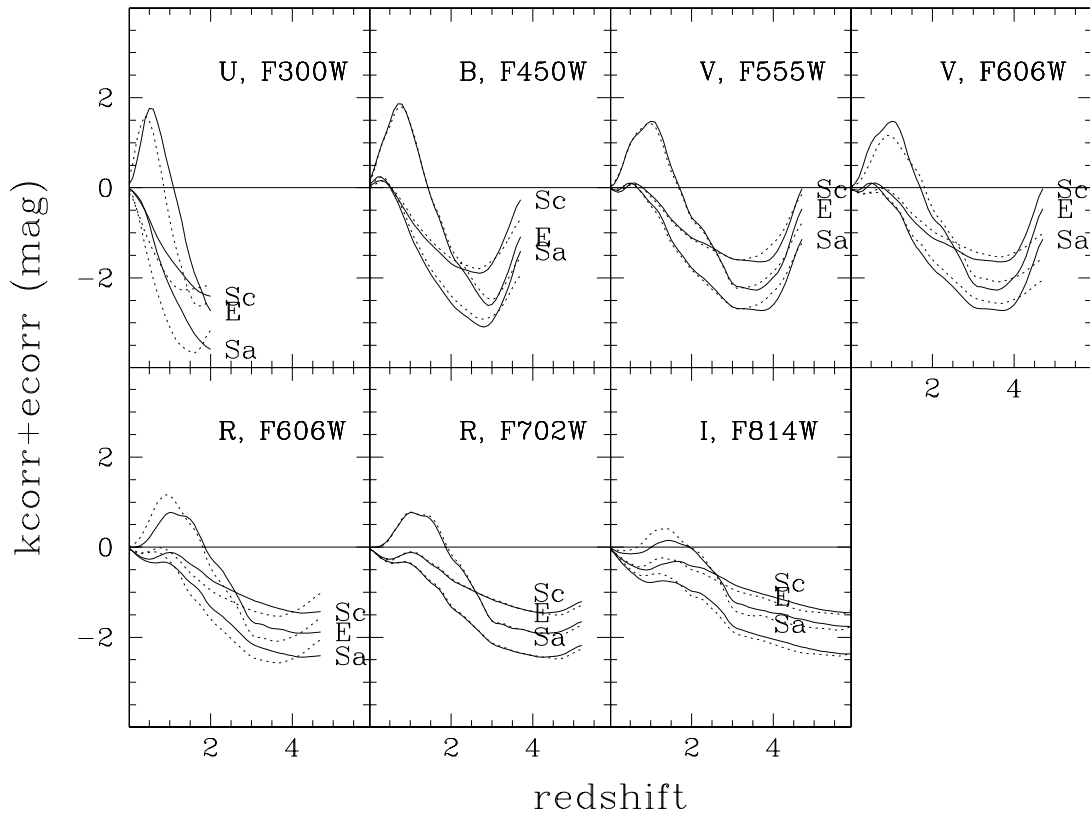


FIG. 14.—Sum of the evolutionary and K -corrections for Johnson/Cousins (solid lines) and WFPC2 filters (dotted lines) shown in Figs. 12 and 13

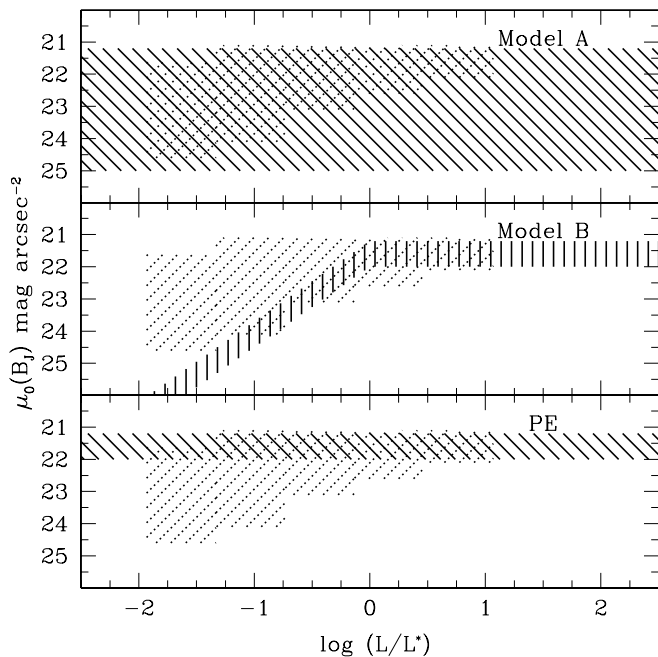


FIG. 15.—Surface brightness distribution as a function of luminosity for the models adopted here (model A, model B, and model PE; *dark hatched regions*). For comparison, the light hatched region shows the surface brightness distribution as a function of luminosity (relative to L^*) as found by Blanton et al. (2001).

berry et al. 1997; Dalcanton et al. 1997; O’Neil & Bothun 2000), these models are taken as illustrative limits on the fraction of low surface brightness galaxies in the local universe. Recent determinations of the number density of galaxies as a function of both luminosity and surface brightness (see, e.g., Blanton et al. 2001 and Cross et al. 2001) are well bracketed by these models: model A allows for too many low surface brightness galaxies, while the PE model clearly allows for too few (see Fig. 15).

As described in Table 2 of Ferguson & McGaugh (1995), each surface brightness distribution model has been paired with a tuned luminosity function so that each model matches the observed morphological distributions and luminosity functions recovered by local redshift surveys. The models include identical distributions in the relative number of galaxies of different Hubble types (E/S0, S0, Sab, Sbc, and Sdm), which are described by bulge-to-disk flux ratios of 1.0, 0.4, 0.3, 0.15, and 0.0, respectively, with small scatter. The bulge components for all galaxies have E-type SEDs, and S0 to Sdm galaxies have disk components with E, Sa, Sb, and Sc-type SEDs, for which we have used the Poggianti (1997) models. Bulges were given $r^{1/4}$ -law light profiles with central surface brightnesses drawn from the empirical relationship found by Sandage & Perelmuter (1990), $\mu_0 = -0.48M_{B_T} + 11.02$. For disk components, we adopted exponential light profiles, with surface brightnesses drawn from the three model distributions for disk galaxies listed above.

We have calculated passive evolution and K -corrections from the population synthesis models and SEDs of Poggianti (1997), shown in Figures 12 and 13, and we have assumed uniform comoving density as a function of redshift in all cases. All models were run with $H_0 = 50$ and $70 \text{ km s}^{-1} \text{ Mpc}^{-1}$ and $(\Omega_M = 0.2, \Omega_\Lambda = 0)$, $(1, 0)$, and $(0.2, 0.8)$. Different values of H_0 have little effect ($<10\%$) on the inte-

grated counts or background. The total background increases for models with larger volume— $(1, 0)$, $(0.2, 0)$, and $(0.2, 0.8)$, in order of increasing volume—but the fractional flux as a function of redshift changes by less than 10% with cosmological model.

All three models underpredict the number counts and integrated flux in observed sources, as expected, and will clearly underpredict the total EBL as illustrated in the passive-evolution model discussed in § 4.2.

5.2. Results

In Figures 16, 17, and 18 we plot the distribution of the total flux from the modeled galaxy populations as a function of redshift, wavelength, and origin, respectively (detectable or undetectable galaxies). Detection limits applied at each bandpass are the 5σ detection limits of the HDF catalog (Williams et al. 1996), with appropriate conversions to the ground-based filter bandpasses, summarized in Table 3. The conversions given in this table include differences in the evolutionary corrections and K -corrections between WFPC2 and $UBVRI$ filters (see Figs. 12–14), which are generally less than 0.3 mag and change by less than 0.1 mag at $z \gtrsim 0.5$. We only consider sources with $V > 23$ mag here, and we assume perfect photometry for sources that meet the detection criteria.

In Figure 16 we show the fraction of the total flux that comes from undetected sources as a function of redshift. For all models, this plot demonstrates that if galaxy populations at higher redshifts are the passively evolving counterparts of those in the local universe, the flux from undetected sources becomes significant by redshifts of $1 < z < 3$. The undetected fraction is the highest in the U band because of the high sky noise and low sensitivity of the F300W HDF images relative to the other bandpasses that define our detection criteria. The detection fractions are similar in B and V , where detection limits and galaxy colors are similar. The fraction of light from undetected sources in I is small at $z < 2$ because of the generally red color of galaxies but increases beyond that redshift because of cosmological effects. Model A, with the largest fraction of low μ_0 galaxies, has the sharpest increase in the undetected EBL with redshift, as expected. A balance between evolutionary and K -corrections at $1 < z < 3$ slow this trend and cause the dip in the fraction of undetected light in B , V , and R . The Lyman limit for each band obviously represents the highest redshift from which one could expect to detect flux.

In Figure 17 we plot the distribution of light with redshift in these models. All three models have roughly the same distribution of $I_{\text{EBL}}(\lambda, z)$ simply because all models employ a uniform comoving number density with redshift and the same passive luminosity evolution. Although we do not intend to realistically predict the redshift distribution of the EBL, we show this plot for comparison with Figure 16 to indicate the redshifts at which the majority of undetected galaxies lie in these models. Looking at Figures 16 and 17 together, it is clear that while 40%–100% of the B -band flux from $z > 3$ is in undetectable sources for all of the models considered, only a small fraction of the total B -band EBL comes from those redshifts. Thus, the majority of the light from unresolved sources comes from $1 < z < 3$ at B for local-type galaxy populations in this scenario.

Figure 18 shows the fraction of EBL23 coming from undetected sources as a function of wavelength. These mod-

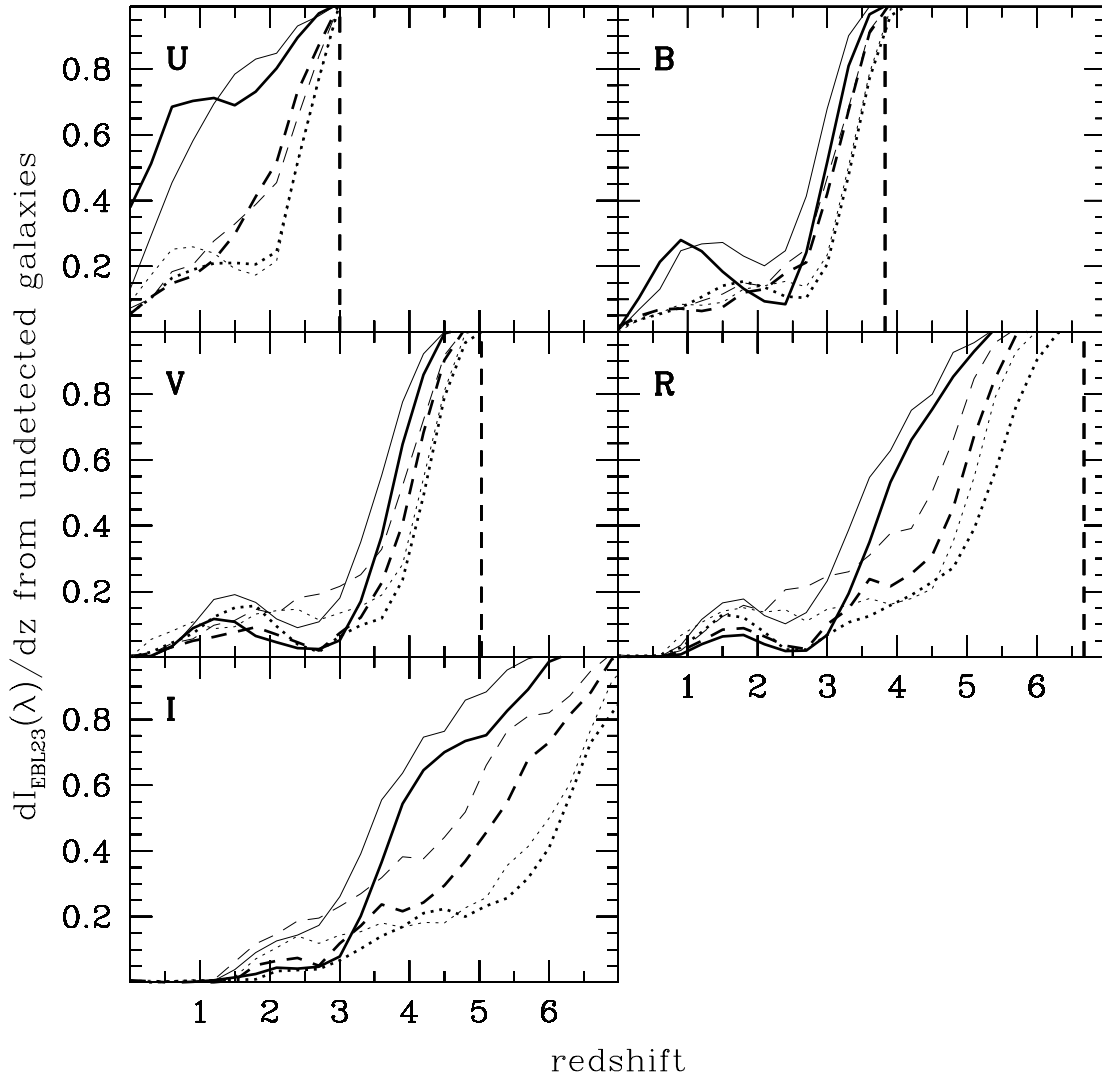


FIG. 16.—EBL from galaxies that are not individually detected in each redshift bin, normalized by the total EBL in each redshift bin plotted for the Johnson/Cousins bandpasses indicated in each panel. Models A, B, and PE are marked with solid, dashed, and dotted lines, respectively. The heavy lines correspond to simulations run with $h = 0.7$, $\Omega_0 = 1.0$, while thin lines correspond to $h = 0.7$, $\Omega_0 = 0.2$. The dotted vertical line in each panel indicates the Lyman limit for the bandpass.

els indicate that 10%–35% of the light from the high redshift counterparts of local galaxy populations would come from (individually) undetected sources in bandpasses between V and I with sensitivity limits similar to the HDF, 15%–40% would come from undetected sources at B , and 20%–70% would come from undetected sources at U . This trend with wavelength (smallest fraction of undetected sources around 5000 Å) follows the trend in the detection limits of the HDF bandpasses, as discussed in § 4.1. Note that the color of the EBL23 is similar to the color of detected galaxies (see Fig. 1) in V and I , as is the 2σ lower limit of min EBL23 (see also Table 2).

We stress again that cosmological surface brightness dimming and the fraction of LSBs in each model are the dominant effects that govern how much light comes from undetected sources, and these effects are independent of wavelength. The passive luminosity evolution corrections, K -corrections, and the HDF-specific detection limits we adopt will determine how the fraction of undetected sources

varies with wavelength. Finally, we note that although the surface brightness distribution of galaxies as a function of redshift is presently unconstrained and may or may not show significant variation with redshift, it is unlikely that the surface brightness distribution at any redshift is significantly more extreme than the distribution bracketed by our models. Bearing these uncertainties in mind, we can use the results of these models to estimate the value of EBL23 based on the min EBL23 (the flux in individually detected galaxies from ensemble aperture photometry) and the undetected fractions summarized above. If the universe is populated by galaxies with surface brightness distributions like those in the local universe, then these models suggest the following values for EBL23: $(2.6\text{--}7.0) \times 10^{-9}$, $(1.0\text{--}1.3) \times 10^{-9}$, and $(0.9\text{--}1.2) \times 10^{-9}$ cgs at U_{300} , V_{555} , and I_{814} , respectively. These ranges are in good agreement with our detected values for EBL23 (see Table 2) and with the estimates of the EBL23 based on the corrected number counts we presented in § 4.1.

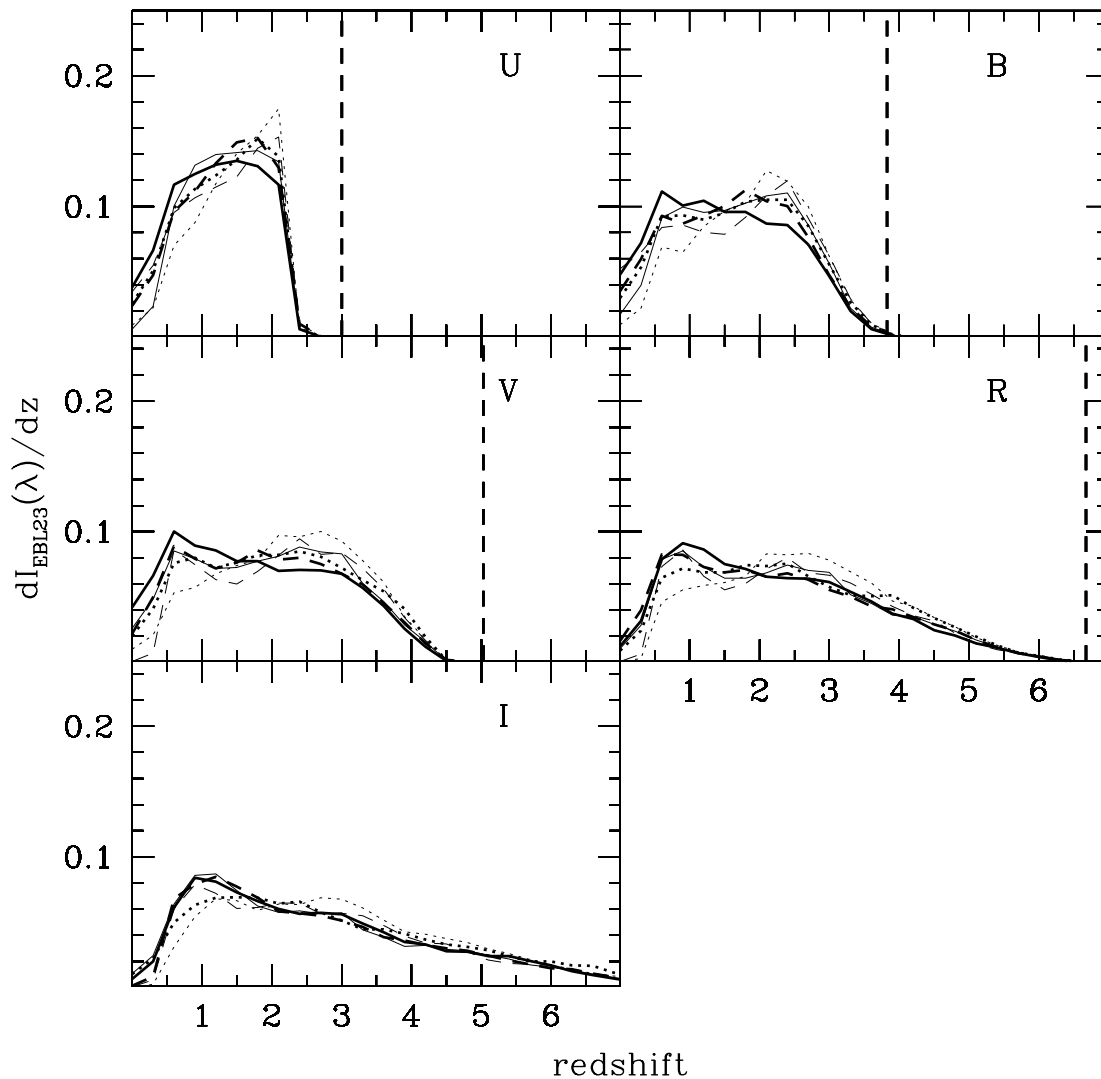


FIG. 17.—Redshift distribution of the EBL—the differential EBL from all galaxies as a function of redshift—normalized by the total EBL in each band plotted for the Johnson/Cousins bandpasses indicated in each panel and the models discussed in the text. Line types correspond to the models as described in the caption of Fig. 16. In this plot, cosmological models are virtually indistinguishable because the fractional volume per redshift bin changes very little with Ω . The dashed vertical line in each plot indicates the redshift corresponding to the Lyman limit for the central wavelength of each bandpass.

6. THE BOLOMETRIC EBL (0.1–1000 μm)

In Figure 19 we plot EBL detections to date together with the integrated light in detectable sources (lower limits to the EBL) in units of νI_ν between 0.1 and 1000 μm .⁶ The DIRBE and FIRAS detections at $\lambda > 100 \mu\text{m}$ and the lower limit from *IRAS*-detected galaxies at 10–100 μm indicate that energy is contained in the far-infrared portion of the spectrum. Given that light from stellar nucleosynthesis is emitted at wavelengths 0.1–10 μm , Figure 19 emphasizes the fact that 30% or more of the light from stellar nucleosynthesis has been redistributed into the wavelength range 10–1000 μm by dust absorption and reradiation and, to a lesser degree, by cosmological redshifting. Realistic estimates of the total energy from stellar nucleosynthesis must therefore be based

⁶ The total energy per unit increment of wavelength is given by $I = \int I_\lambda d\lambda = \int \lambda I_\lambda d \ln \lambda$. By plotting energy as $\lambda I_\lambda = \nu I_\nu$ against $\log \lambda$, the total energy contained in the spectrum as a function of wavelength is proportional to the area under the curve. We give λI_λ in standard units of $\text{nW m}^{-2} \text{sr}^{-1}$, equivalent to $10^{-6} \text{ ergs s}^{-1} \text{ cm}^{-2} \text{ sr}^{-1}$.

on the bolometric EBL from the UV to IR. In lieu of accurate measurements in the mid-IR range, realistic models of dust obscuration and the dust re-emission spectrum (dust temperature) are needed. To discuss the optical EBL in the context of star formation, we must therefore first estimate the bolometric EBL based on the optical EBL detections presented here and current measurements in the far-IR. We do so in the following section.

6.1. Models

Efforts to predict the intensity and spectrum of the EBL by Partridge & Peebles (1967) and Harwit (1970) began with the intent of constraining cosmology and galaxy evolution. Tinsley (1977, 1978) developed the first detailed models of the EBL explicitly incorporating stellar initial mass functions (IMFs), star formation efficiencies, and stellar evolution. Most subsequent models of the EBL have focused on integrated galaxy luminosity functions with redshift-dependent parameterization, with particular attention paid to dwarf and low surface brightness galaxies (see discussions

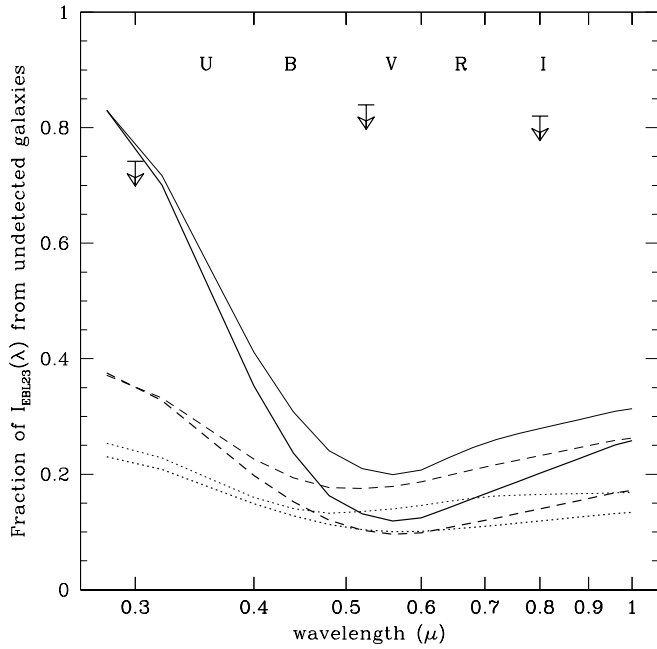


FIG. 18.—Fraction of the EBL that comes from undetected galaxies as predicted by our models. Line types are as in Fig. 16. The arrows show the upper limits on the fraction of the EBL that might come from undetected galaxies based on the EBL detections summarized in § 3 and Table 2. These arrows show the ratio of flux recovered by ensemble photometry (from resolved galaxies) and the 2σ upper limits of our EBL detection. See § 5.2 for discussion.

in Guiderdoni & Rocca-Volmerange 1990; Yoshii & Takahara 1988; Väisänen 1996).

More recent efforts have focused on painting a detailed picture of star formation history and chemical enrichment based on the evolution of resolved sources. The evolution of the UV luminosity density can be measured directly from galaxy redshift surveys (see, e.g., Lilly et al. 1996; Treyer et al. 1998; Cowie et al. 1999; Steidel et al. 1999; Sullivan et al. 2000), from which the star formation rate with redshift $\dot{\rho}_*(z)$ can be inferred for an assumed stellar IMF. The mean properties of QSO absorption systems with redshift can also be used to infer $\dot{\rho}_*(z)$, based on either the decrease in H I column density with decreasing redshift (under the assumption that the disappearing H I is being converted into stars) or the evolution in metal abundance for an assumed IMF and corresponding metal yield (see, e.g., Pettini et al. 1994; Lanzetta, Wolfe, & Turnshek 1995; Pei & Fall 1995). Estimates of the star formation rate at high redshift have also come from estimates of the flux required to produce the proximity effect around QSOs (see, e.g., Gunn & Peterson 1965; Tinsley 1972; Miralda-Escudé & Ostriker 1990). Using these constraints, the full spectrum of the EBL can then be predicted from the integrated flux of the stellar populations over time.

Unfortunately, all methods for estimating $\dot{\rho}_*(z)$ contain significant uncertainties. The star formation rate deduced from the rest-frame UV luminosity density is very sensitive to the fraction of high-mass stars in the stellar initial mass function (IMF) and can vary by factors of 2–3 depending on the value chosen for the low-mass cutoff (see Leitherer 1999; Maeder 1992). Aside from the large uncertainties in the measured UV luminosity density due to incompleteness, resolved sources at high redshift are biased toward objects with dense star formation and may therefore paint an

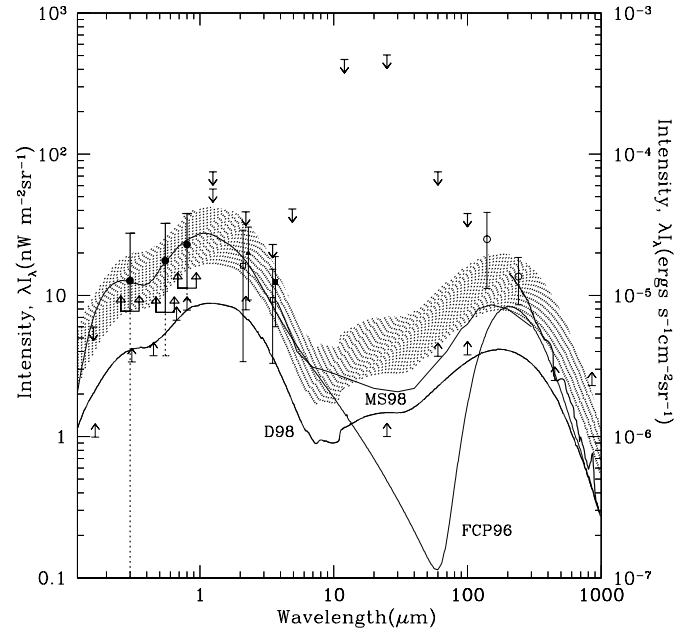


FIG. 19.—EBL detections, limits, and models as a function of wavelength. The filled circles show the EBL detections with 2σ error bars and lower-limit symbols as defined in Fig. 8. Also plotted are lower limits from Armand, Millard, & Deharveng (1994) at 2000 \AA , the HDF (Williams et al. 1996), Gardner et al. (1997) at $2.2\text{ }\mu\text{m}$, *IRAS* (Hacking & Soifer 1991) at $10\text{--}100\text{ }\mu\text{m}$, and Blain et al. (1999) at 450 and $850\text{ }\mu\text{m}$. These lower limits are based on the integrated flux in detected sources at each wavelength. Upper limits marked in bold are from Hurwitz, Bowyer, & Martin (1991) at 1600 \AA and DIRBE (Hauser et al. 1998). The open circles indicate DIRBE detections. The heavy line at $125\text{--}1000\text{ }\mu\text{m}$ shows the FIRAS detection (Fixsen et al. 1998). Detections in the near-IR are from Wright (2000, *filled triangle*), Gorjian et al. (2000, *open squares*), and Wright & Reese (2000, *filled square*). The lines that indicate models are all labeled and are from Malkan & Stecker (1998, MS98), Dwek et al. (1998, D98), and Fall et al. (1996, FCP96) as described in § 6. The shaded region shows the D98 model rescaled to match the range allowed by our EBL detections.

incomplete picture of the high- z universe. Also, large corrections for extinction due to dust must be applied to convert an observed UV luminosity density into a star formation rate (Calzetti 1997).

The star formation rate inferred from QSO absorption systems, whether from consumption of H I or increasing metal abundance, is also subject to a number of uncertainties. In all cases, samples may be biased against the systems with the most star formation, dust, and metals: dusty foreground absorbers will obscure background QSOs, making the foreground systems more difficult to study. In addition, large-scale outflows, a common feature of low-redshift starburst galaxies, have recently been identified in the high-redshift rapidly star-forming Lyman break galaxies (Pettini et al. 2000), suggesting that changes in the apparent gas and metal content of such systems with redshift may not have a simple relationship to $\dot{\rho}_*(z)$ and the metal production rate. The mass-loss rate in one such galaxy appears to be as large as the star formation rate, and the recent evidence for C IV in Ly α forest systems with very low H I column densities ($\lesssim 10^{14}\text{ cm}^{-2}$) suggests that dilution of metals over large volumes may cause underestimates in the apparent star formation rate derived from absorption line studies (see Ellison et al. 1999; Pagel 1999; Pettini 1999 and references therein).

Finally, regarding the predicted spectrum of the EBL, the efforts of Fall, Charlot, & Pei (1996) and Pei, Fall, &

Hauser (1999) emphasize the need for a realistic distribution of dust temperatures in order to obtain a realistic near-IR spectrum.

With these considerations in mind, we have adopted an empirically motivated model of the spectral shape of the EBL from Dwek et al. (1998, hereafter D98). This model is based on $\dot{\rho}_*(z)$ as deduced from UV-optical redshift surveys and includes explicit corrections for dust extinction and reradiation based on empirical estimates of extinction and dust temperature distributions at $z = 0$. The comoving luminosity density can then be expressed explicitly as the sum of the unattenuated stellar emission $\epsilon_s(\nu, z)$ and the dust emission per unit comoving volume $\epsilon_d(\nu, z)$. Equation (1) then becomes

$$I(\lambda, 0) = \int_0^z \frac{[\epsilon_s(\nu, z) + \epsilon_d(\nu, z)] dV_C(z)}{4\pi D_L(z)^2}. \quad (3)$$

D98 estimate the ratio $\epsilon_d(\lambda, 0)/\epsilon_s(\lambda, 0)$ by comparing the UV-optical luminosity functions of optically detected galaxies with IR luminosity function of *IRAS*-selected sources. Using values of $\mathcal{L} = (1.30 \pm 0.7) \times 10^8 L_\odot \text{ Mpc}^{-3}$ for the local stellar luminosity density at 0.1–10 μm and $\mathcal{L} = 0.53 \times 10^8 L_\odot \text{ Mpc}^{-3}$ for the integrated luminosity density of *IRAS* sources, Dwek et al. obtain $\epsilon_d(\lambda, 0)/\epsilon_s(\lambda, 0) \sim 0.3$. The redshift-independent dust opacity is assumed to be an average Galactic interstellar extinction law normalized at the *V*-band to match this observed extinction. D98 then calculate the EBL spectrum using the UV-optical observed $\dot{\rho}_*(z)$, a Salpeter IMF ($0.1 M_\odot < M < 120 M_\odot$), stellar evolutionary tracks from Bressan et al. (1993), Kurucz stellar atmosphere models for solar metallicity, redshift-independent dust extinction, and dust re-emission matching the SED of *IRAS* galaxies.

The starting point UV-optical $\dot{\rho}_*(z)$ for this model is taken from Madau et al. (1998), which underpredicts the detected optical EBL presented in Paper I (see § 4.3). While D98 discuss two models that include additional star formation at $z \gtrsim 1$, the additional mass is all in the form of massive stars that radiate instantaneously and are entirely dust-obscured, resulting in an ad hoc boost to the far-IR EBL. We instead simply scale the initial Dwek et al. model by 2.2 to match the 2σ lower limit of our EBL detections and 4.7 to match the 2σ upper limit in order to preserve the consistency of the D98 model with the observed spectral energy density at $z = 0$. In that any emission from $z > 1$ will have a redder spectrum than the mean EBL, simply scaling in this way will produce a spectrum that is too blue. However, as discussed in § 4.2, it is also possible that the $z < 0.5$ UV luminosity density has been underestimated by optical surveys so that the bluer spectrum we have adopted may be appropriate. Note that the resulting model is in excellent agreement with recent near-IR results at 2.2 and 3.5 μm (Wright & Reese 2000; Gorjian, Wright, & Chary 2000; Wright 2000) and also with the DIRBE and FIRAS results in the far-IR. Adopting this model, we estimate that the total bolometric EBL is $100 \pm 20 \text{ nW m}^{-2} \text{ sr}^{-1}$, where errors are 1σ errors associated with the fit of that template to the data.

Because of the corrections that account for the redistribution by dust of energy into the IR portion of the EBL, the star formation rate implied by the unscaled (or scaled) D98 model is 1.5 (or 3.3–7.1) times larger than the star formation rate adopted by Madau et al. (1998). The dust corrections

used by Steidel et al. (1999) produce a star formation rate that is roughly 3 times larger than that used in the unscaled D98 model, slightly smaller than the scaling range adopted here, which is consistent with the fact that the CFRS and Steidel et al. (1999) luminosity densities are slightly below our minimum values for the EBL, as discussed in § 4.2.

6.2. Energy from Accretion

As mentioned briefly in § 1, another significant source of energy at UV to far-IR wavelengths is accretion onto black holes in AGNs and QSOs. The total bolometric flux from accretion can be estimated from the local mass function of black holes at the centers of galaxies for an assumed radiation efficiency and total accreted mass. Recent surveys find $M_{\text{bh}} \approx 0.005 M_{\text{sph}}$, in which M_{sph} is the mass of the surrounding spheroid and M_{bh} is the mass of the central black hole (Richstone et al. 1998; Magorrian et al. 1998; Salucci et al. 1999; van der Marel 1999). Following Fabian & Iwasawa (1999), the energy density in the universe from accretion is given by

$$\mathcal{E}_{\text{bh}} = 0.005 \Omega_{\text{sph}} \rho_{\text{crit}} c^2 \frac{\eta_{\text{bh}}}{(1+z_e)}, \quad (4)$$

in which η_{bh} is the radiation efficiency, Ω_{sph} is the observed mass density in spheroids in units of the critical density ρ_{crit} , and $(1+z_e)$ compensates for the energy lost because of cosmic expansion since the emission redshift z_e . The bolometric flux from accretion is then

$$I_{\text{bh}}^{\text{bol}} = \frac{c}{4\pi} \frac{\mathcal{E}_{\text{bh}}}{(1+z_e)} \sim 10 h \text{ nW m}^{-2} \text{ sr}^{-1} \quad (5)$$

for $\eta_{\text{bh}} \sim 0.1$, $z_e \sim 2$, $\rho_{\text{crit}} = 2.775 \times 10^{11} h^2 M_\odot \text{ Mpc}^{-3}$, $H_0 = 100 h \text{ km s}^{-1} \text{ Mpc}^{-1}$, and $\Omega_{\text{sph}} \sim 0.0018_{-0.00085}^{+0.0012} h^{-1}$ (Fukugita, Hogan, & Peebles 1998, hereafter FHP98).

The observed X-ray background (0.1–60 keV) is $\sim 0.2 \text{ nW m}^{-2} \text{ s}^{-1}$. The large discrepancy between the detected X-ray flux and the estimated flux from accretion has led to suggestions that 85% of the energy estimated to be generated from accretion takes place in dust-obscured AGN and is emitted in the thermal IR (see discussions in Fabian 1999). Further support for this view comes from the fact that most of the soft X-ray background (below 2 keV) is resolved into unobscured sources (i.e., optically bright QSOs), while most of the hard X-ray background is associated with highly obscured sources (Mushotzky et al. 2000). Photoelectric absorption can naturally account for the selective obscuration of the soft X-ray spectrum. Best estimates for the fraction of the far-IR EBL that can be attributed to AGNs are then less than $10 h \text{ nW m}^{-2} \text{ sr}^{-1}$, or less than 30% of the observed IR EBL. This is in good agreement with estimates of the flux from a growing central black hole relative to the flux from stars in the spheroid based on arguments for termination of both black hole accretion and star formation through wind-driven ejection of cool gas in the spheroid (Silk & Rees 1998; Fabian 1999; Blandford 1999). Together, these studies suggest that less than 15% of the bolometric EBL comes from accretion onto central black holes.

7. STELLAR NUCLEOSYNTHESIS: Ω_* AND $|Z|$

The bolometric flux of the EBL derived in § 6.1 is a record of the total energy produced in stellar nucleosynthesis in the

universe and so can be used to constrain estimates of the baryonic mass that has been processed through stars. The relationship between processed mass and background flux depends strongly on the redshift dependence of star formation and on the stellar IMF but is only weakly dependent on the assumed cosmology for the reasons discussed in §§ 4.2 and 5.

As an illustrative case, we can obtain a simple estimate of the total mass processed by stars by assuming that all stars were formed in a single burst at an effective redshift z_e and that all the energy from that burst was emitted instantaneously. The assumption of instantaneous emission does not strongly affect the result because most of the light from a stellar population is emitted by hot, short-lived stars in the first ~ 10 Myr. The integrated EBL at $z = 0$ in equation (1) then simplifies to

$$I_*^{\text{bol}} = \frac{c}{4\pi(1+z_e)} \mathcal{E}_* , \quad (6)$$

in which \mathcal{E}_* is the bolometric energy density from stellar nucleosynthesis and $(1+z_e)$ compensates for energy lost to cosmic expansion. In the case of instantaneous formation and emission, \mathcal{E}_* can be expressed in terms of the total energy released in the nucleosynthesis of He and heavier elements:

$$\mathcal{E}_* = \Omega_* \rho_{\text{crit}} c^2 \eta (\Delta Y + Z) , \quad (7)$$

in which η (~ 0.0075) is the mean conversion efficiency of energy released in nuclear reactions and ΔY and Z are the mass fractions of ^4He and metals. Inverting equation (6), the total baryonic mass processed through stars in this model can be derived from a measurement of the bolometric EBL using the expression:

$$\Omega_* = \frac{4\pi(1+z_e)}{c^3 \eta \rho_{\text{crit}}} \frac{I_*^{\text{bol}}}{\langle \Delta Y + Z \rangle} . \quad (8)$$

We can bracket a reasonable range for $\langle \Delta Y + Z \rangle$ by assuming the solar value as a lower limit and the mass-weighted average of the metal conversion fraction in E/S0 and spiral galaxies as the upper limit.⁷ Assuming a 32 ratio of E/S0 to Sabc galaxies (Persic & Salucci 1992), we find $\langle \Delta Y + Z \rangle = 0.25 \pm 0.15$. For $z_e = 1.5$, the total baryonic mass processed through stars corresponding to a bolometric EBL of 100 ± 20 nW m⁻² sr⁻¹ is then $\Omega_* = 0.0030(\pm 0.0019) h^{-2}$ in units of the critical density, or $0.16 (\pm 0.10) \Omega_B$ for $\Omega_B = 0.019(\pm 0.001) h^{-2}$ (Burles & Tytler 1998). Again, this calculation assumes a single redshift for star formation with all energy radiated instantaneously at the redshift of formation.

The true history of star formation is obviously quite different from this illustrative case. For time-dependent emission and formation, the bolometric EBL is the integral of

⁷ Solar values of ΔY and Z are 0.04 and 0.02, respectively, implying $DY/DZ = 2$. Interstellar absorption measurements of DY/DZ in the solar neighborhood are closer to the range 3–4, implying $\Delta Y \sim 0.07$. Helium white dwarfs contribute an additional 10% of the local stellar mass to the estimate of ΔY (Fleming, Liebert, & Green 1986), so that we have $\langle \Delta Y + Z \rangle = 0.07 + 0.02 + 0.1 \sim 0.2$ as a local estimate for systems with solar metallicity. This is similar to estimates for other local spiral galaxies. Estimates for E/S0 galaxies are as high as 0.5 (Pagel 1997, p. 312). (Note that the He mass produced in stars is written as ΔY to distinguish it from the total He mass, which includes a primordial component.)

the comoving luminosity density corresponding to realistic age- and redshift-dependent emission (see eq. [1]). For comparison, instantaneous formation at the same redshift assumed above ($z_e = 1.5$) with a modified Salpeter IMF and time-dependent emission based on SEDs from Buzzoni (1995) would imply $\Omega_* = 0.0037(\pm 0.0007) h^{-2}$ for our estimate of the bolometric EBL (for details, see Madau et al. 1998 and Madau & Pozzetti 2000, hereafter MP00). The mean of this estimate is about 20% higher than that from the instantaneous formation and emission model discussed above. The two models are very similar because the vast majority of energy from a stellar population is emitted in the first ~ 10 Myr. The quoted uncertainty is smaller than for our illustrative model because the error range reflects only the uncertainty in our estimate of the bolometric EBL and no uncertainties in the adopted IMF.

For the same IMF and SEDs, a redshift-dependent star formation rate for $0 < z < 4$ based on the observed UV luminosity density and taking dust obscuration into account (see Steidel et al. 1999) would imply that almost twice as much mass is processed through stars than in the instantaneous formation model above (MP00). Relative to the instantaneous-formation models, the same bolometric EBL flux corresponds to a larger value of Ω_* when we consider time-dependent star formation because more of the emission occurs at higher redshifts, resulting in greater energy losses to cosmic expansion. For our estimate of $I_{\text{EBL}}^{\text{bol}}$ and the calculations of MP00 discussed above, we therefore estimate that total mass fraction processed through stars is $\Omega_* = 0.0062(\pm 0.0012) h^{-2}$ or $0.33 \pm 0.07 \Omega_B$. We adopt this value for the remainder of the paper.

For this value of the total processed mass, we can calculate the corresponding metal mass that is produced in stellar nucleosynthesis. To do so requires an estimate of the metal yield—the mass fraction of metals returned to the interstellar medium relative to the mass remaining in stars and stellar remnants. Best estimates of the metal yield y_Z lie between 0.01 (corresponding to a Scalo IMF) and 0.034 (as observed in the Galactic bulge; Pagel 1987, 1999). These values incorporate the full range predicted by IMF models and observations (see Woosley & Weaver 1995; Tsujimoto et al. 1995; Pagel & Tautvaisiene 1997; Pagel 1997, p. 312). For $Z_\odot = 0.017$ (Grevesse, Noels, & Sauval 1996), this metal yield range in solar units is $y_Z = 1.3 \pm 0.7 Z_\odot$. If the mass fraction remaining in stars and stellar remnants is f , then the predicted metal mass density is given by

$$\Omega_Z = f y_Z \Omega_* , \quad (9)$$

which gives $\Omega_Z = 0.0040(\pm 0.0022) h^{-2} Z_\odot$, or $\Omega_Z = 0.24(\pm 0.13) Z_\odot \Omega_B$, for an assumed lock-up fraction of $f = 0.5$.

Note that we have assumed that the full flux of the EBL is due to stellar nucleosynthesis in the above calculations of Ω_* and Ω_Z . If $\lesssim 10 h$ nW m⁻² sr⁻¹ of the IR EBL is due to AGNs, as estimated in § 6.2, then the energy emitted by stars is smaller by about 7%, and the inferred mass fractions are then smaller by about 7% as well.

7.1. Comparison with Other Observations

The total mass processed by stars is not a directly observable quantity because some fraction of the processed mass will be hidden in stellar remnants or recycled back into the interstellar medium. Estimates of recycling fraction range

from 30% to 50% for various IMF models (see discussions in Pagel 1997, p. 312), but the cumulative effect of many generations of star formation and repeated recycling is difficult to estimate. Firm lower and upper limits for Ω_* are, however, directly observable: the observed mass in stars and stellar remnants at $z \sim 0$ is a lower limit to the total mass that has been processed through stars, and the total baryon fraction from Big Bang nucleosynthesis is an upper limit. FHP98 estimate the mass fraction in stars and stellar remnants at $z \sim 0$ to be $\Omega_{\text{stars}} = 0.0025(\pm 0.001) h^{-1}$, corresponding to a mass-to-light ratio of $(M/L)_B \sim 5.9(M/L)_\odot$. In units of Ω_B , this lower limit is $\Omega_{\text{stars}} = 0.13(\pm 0.05) h \Omega_B$. Our estimate of the total mass fraction processed through stars, $\Omega_* = 0.33(\pm 0.07)\Omega_B$, is comfortably above this lower limit and is, obviously, less than the upper limit—the total baryon mass fraction from Big Bang nucleosynthesis and deuterium measurements.

We can also compare the metal mass fraction predicted by the EBL with the observed mass fraction in gas, stars, and stellar remnants in the local universe. Based on recent estimates by FHP98, $\sim 80\%$ of the observed baryons at $z \sim 0$ are located in the intracluster gas of groups and clusters, 17% are in stars and stellar remnants, and only 3% are in neutral atomic and molecular gas. The observed metal mass fraction in hot intracluster gas has been estimated to be at least $0.33 Z_\odot$ for rich galaxy clusters and $0.25\text{--}1 Z_\odot$ in groups based on X-ray observations of Fe features (Renzini 1997; Mushotzky & Loewenstein 1997). More recent estimates from Buote (1999, 2000) based on more detailed models of the temperature distribution of the intracluster gas have found values closer to $1 Z_\odot$ in several clusters and elliptical galaxies. For a total cluster and group gas mass density of $\Omega_{\text{gas}} = 0.011^{+0.013}_{-0.005} h^{-1}$ (FHP98) and assuming a metal mass fraction of $0.65 \pm 0.35 Z_\odot$ for clusters and groups of all masses, the observed metal mass fraction in clusters is $\Omega_{Z,\text{gas}} = 0.007^{+0.009}_{-0.005} h^{-1} Z_\odot$. Repeating this exercise for the stellar component, we assume that the metallicity of stars at $z \sim 0$ is roughly solar ($1.0 \pm 0.25 Z_\odot$) and that the mass density in stars is $\Omega_{\text{stars}} = 0.0025(\pm 0.001) h^{-1}$. The total metal mass in stars and stellar remnants locally is then $\Omega_{Z,\text{star}} = 0.0025(\pm 0.001) h^{-1} Z_\odot$. The total metal mass fraction in the local universe is then $\Omega_Z = \Omega_{Z,\text{star}} + \Omega_{Z,\text{gas}} = 0.0095^{+0.010}_{-0.006} h^{-1} Z_\odot$, or $0.50^{+0.52}_{-0.32} h Z_\odot \Omega_B$. This estimate is consistent with the value indicated by the bolometric EBL, $0.24(\pm 0.13) Z_\odot \Omega_B$, as calculated above.

8. SUMMARY AND CONCLUSIONS

Based on surface photometry from *HST*/WFPC2 and simultaneous ground-based surface spectrophotometry from the Las Campanas Observatory, we find mean values for the flux of the EBL23 (the background light from sources fainter than $V = 23$ AB mag) as follows: $I_{F300W} = 4.0 \pm 2.5$, $I_{F555W} = 2.7 \pm 1.4$, and $I_{F814W} = 2.2 \pm 1.0$ in units of 10^{-9} cgs, where uncertainties quoted are 1σ combined statistical and systematic errors. These results are presented in detail in Paper I and are summarized in § 3. Adding in the flux from sources brighter than $V = 23$ AB mag (see Table 2), we find that the total EBL flux is $I_{F300W} = 4.3 \pm 2.6$, $I_{F555W} = 3.2 \pm 1.5$, and $I_{F814W} = 2.9 \pm 1.1$ cgs.

In the context of these measurements of the EBL, we have discussed constraints on the slope of number counts, the luminosity density as a function of redshift, the fraction of

galaxies that lie below current surface brightness detection limits, and the history of stellar nucleosynthesis and metal production in the universe. We reach the following principle conclusions:

1. We find that the corrected number counts at V and I magnitudes fainter than 23 AB mag obey the relation $N \propto 10^{\alpha m}$, with $\alpha = 0.33 \pm 0.01$ and $\alpha = 0.34 \pm 0.01$, respectively, which is consistent with the slope found at brighter magnitudes (see, e.g., Smail et al. 1995; Tyson 1988). This is significantly steeper than the slope of the raw HDF number counts ($\sim 0.24 \pm 0.1$ at $V > 23$ AB mag and $\sim 0.22 \pm 0.1$ at $I > 23$ AB mag). In contrast with the raw counts, the corrected counts show no decrease in slope to the detection limit. If we integrate the corrected number counts down to an apparent magnitude corresponding roughly to a dwarf galaxy ($M_V \sim -10$ mag) at $z \sim 3$, $V \sim 38$ AB mag, we obtain a total flux of 1.2×10^{-9} cgs in both V and I . This is 1.2σ below the mean EBL23 flux we estimate at $V_{606}(I_{814})$, suggesting that number counts would need to be steeper over some range in apparent magnitude fainter than the current detection limits in order to obtain the mean EBL flux we detect or that the value of EBL23 is roughly $\sim 1 \sigma$ below our mean detections at V and I .

2. Based on a local luminosity density consistent with Loveday et al. (1992), passive evolution in the luminosity density of galaxies underpredicts the EBL by factors of roughly 3, 2, and 2 at U_{300} , V_{555} , and I_{814} , respectively. Note, however, that if the local luminosity density is a factor of 2 higher than the Loveday et al. values we have adopted here, as found by Blanton et al. (2001), then passive evolution agrees with the flux in resolved galaxies (min EBL23) and with our mean EBL detections to within 1σ . The mean detected EBL therefore requires stronger evolution in the luminosity density than passive evolution will produce; however, the exact form of that evolution is not well constrained by our results.

Adopting the local luminosity density assumed by Lilly et al. (1996, CFRS), the 1σ upper limits of the cumulative flux measured by Lilly et al. from redshifts $0 < z < 1$ is smaller than the flux in resolved sources by more than a factor of 2: this fact alone demonstrates that significant flux must be contributed by galaxies at redshifts $z > 1$. If we adopt $\mathcal{L}(\lambda, z) \propto (1+z)^{\beta(\lambda)}$ for the luminosity density at $0 < z < 1$ based on the Lilly et al. results, then constant luminosity density at $z > 1$, such as suggested by Steidel et al. (1999), is consistent with the detected flux in sources at V_{555} and I_{814} and with the detected EBL at U_{300} . At the upper limit of the EBL detections, we find that the luminosity density can continue to rise as a power law to $z \sim 2.5$ without overpredicting the EBL.

3. We have modeled the effects of cosmological K -corrections, passive evolution, and $(1+z)^4$ cosmological surface brightness dimming on the detectability of local-type galaxy populations as a function of redshift. For these models, we have adopted the spatial resolution and surface brightness limits of the HDF. For models that bracket the observed surface brightness distribution of galaxies in the local universe, we find that roughly 10%–40% of the EBL from galaxies fainter than $V \sim 23$ (i.e., those sampled in an HDF-sized image) comes from galaxies that are, at present, individually undetectable at wavelengths $\lambda > 4500$ Å, and roughly 20%–70% comes from individually undetected galaxies at $\lambda < 4500$ Å. Most of the flux from a local-type

galaxy population located at $z = 3$ would come from sources that would not be individually detected in the HDF. Our models indicate that the true EBL is likely to be between the mean detected EBL23 values and the 1σ lower limits of those detections at V and I and within $\pm 1\sigma$ at U .

4. Scaling the model of the bolometric EBL derived by D98, which is based on a combined UV-optical estimate of the star formation rate and a model for dust obscuration and re-emission based on the spectrum of *IRAS* sources, we find that the optical EBL we detect corresponds to a total bolometric EBL (0.1–1000 μm) of $100 \pm 20 \text{ nW m}^{-2} \text{ sr}^{-1}$.

5. From this estimate of the total bolometric EBL, we estimate that the total baryonic mass processed through stars is $\Omega_* = 0.0062(\pm 0.0012) h^{-2} = 0.33(\pm 0.07)\Omega_B$ and

that the mean metal mass density in the universe is $\Omega_Z = 0.0040(\pm 0.0022) h^{-2} Z_\odot = 0.24(\pm 0.13) Z_\odot \Omega_B$ for $\Omega_B = 0.019(\pm 0.001) h^{-2}$ (Burles & Tytler 1998). These estimates are consistent with limits from other observational constraints.

We would like to thank the referee, M. Bershadsky, for detailed and helpful comments. We also thank R. Carlberg, J. Dalcanton, E. Dwek, P. Madau, R. Marzke, J. X. Prochaska, T. Small, and I. Smail for helpful discussions. This work was supported by NASA through grants NAG LTSA 5-3254 and GO-05968.01-94A to W. L. F. and by NASA through Hubble Fellowship grant HF-01088.01-97A awarded by STScI to R. A. B.

REFERENCES

- Armand, C., Milliard, B., & Deharveng, J. M. 1994, *A&A*, 284, 12
 Bernstein, R. A., Freedman, W. L., Madore, B. F. 2002a, *ApJ*, 571, 56 (Paper I)
 ———. 2002b, *ApJ*, 571, 85 (Paper II)
 Bertin, E., & Arnouts, S. 1996, *A&AS*, 117, 393
 Blain, A. W., Kneib, J.-P., Ivison, R. J., & Smail, I. 1999, *ApJ*, 512, L87
 Blandford, R. 1999, in *ASP Conf. Ser. 182, Galactic Dynamics*, ed. D. Merritt, M. Valluri, & J. Sellwood (San Francisco: ASP), 87
 Blanton, M. R., et al. 2001, *AJ*, 121, 2358
 Bond, J. R., Carr, B. J., & Hogan, C. J. 1986, *ApJ*, 306, 428
 ———. 1991, *ApJ*, 367, 420
 Boyle, B. J., & Terlevich, R. J. 1998, *MNRAS*, 293, L49
 Bressan, A., Fagotto, F. D., Bertelli, G., & Chiosi, C. 1993, *A&AS*, 100, 647
 Buote, D. A. 1999, *MNRAS*, 309, 685
 ———. 2000, *MNRAS*, 311, 176
 Burles, S., & Tytler, D. 1998, *ApJ*, 507, 732
 Buzzoni, A. 1995, *ApJS*, 98, 69
 Calzetti, D. 1997, *AJ*, 113, 162
 Cowie, L. L., Songaila, A., & Barger, A. J. 1999, *AJ*, 118, 603
 Cross, N., et al. 2001, *MNRAS*, 324, 825
 Dalcanton, J. J. 1998, *ApJ*, 495, 251
 Dalcanton, J. J., Spergel, D. N., Gunn, J. E., Schmidt, M., & Schneider, D. P. 1997, *AJ*, 114, 635
 Davies, J. I. 1990, *MNRAS*, 244, 8
 de Jong, R. S., & Lacey, C. 2000, *ApJ*, 545, 781
 Disney, M. 1976, *Nature*, 263, 573
 Disney, M., & Phillipps, S. 1983, *MNRAS*, 205, 1253
 Dwek, E., et al. 1998, *ApJ*, 508, 106 (D98)
 Ellison, S. L., Lewis, G. F., Pettini, M., Chaffee, F. H., & Irwin, M. J. 1999, *ApJ*, 520, 456
 Fabian, A. C. 1999, *MNRAS*, 308, L39
 Fabian, A. C., & Iwasawa, K. 1999, *MNRAS*, 303, L34
 Fall, S. M., Charlot, S., & Pei, Y. C. 1996, *ApJ*, 464, L43
 Fall, S. M., & Pei, Y. C. 1989, *ApJ*, 337, 7
 Ferguson, H. C., & McGaugh, S. S. 1995, *ApJ*, 440, 470
 Fixsen, D. J., Dwek, E., Mather, J. C., Bennet, C. L., & Shafer, R. A. 1998, *ApJ*, 508, 123
 Fleming, T. A., Liebert, J., & Green, R. F. 1986, *ApJ*, 308, 176
 Fukugita, M., Hogan, C. J., & Peebles, P. J. E. 1998, *ApJ*, 503, 518 (FHP98)
 Fukugita, M., Shimasaku, K., & Ichikawa, T. 1995, *PASP*, 107, 945
 Gardner, J. P., Sharples, R. M., Carrasco, B. E., & Frenk, C. S. 1996, *MNRAS*, 282, L1
 Gardner, J. P., Sharples, R. M., Frenk, C. S., & Carrasco, B. E. 1997, *ApJ*, 480, L99
 Gorjian, V., Wright, E. L., & Chary, R. R. 2000, *ApJ*, 536, 550
 Grevesse, N., Noels, A., & Sauval, A. J. 1996, in *ASP Conf. Ser. 99, Cosmic Abundances*, ed. S. Holt & G. Sonneborn (San Francisco: ASP), 117
 Guiderdoni, B., & Rocca-Volmerange, B. 1990, *A&A*, 227, 362
 Gunn, J. E., & Peterson, B. A. 1965, *ApJ*, 142, 1633
 Hacking, P. B., & Soifer, B. T. 1991, *ApJ*, 367, L49
 Hall, P., & Mackay, C. D. 1984, *MNRAS*, 210, 979
 Harwit, M. 1970, *Nuovo Cimento*, 2, 253
 Hauser, M. G., et al. 1998, *ApJ*, 508, 25
 Ho, L. C., Filippenko, A. V., & Sargent, W. L. W. 1997a, *ApJS*, 112, 315
 ———. 1997b, *ApJ*, 487, 568
 Hogg, D. W., Pahre, M. A., McCarthy, J. K., Cohen, J. G., Blandford, R., Smail, I., & Soifer, B. T. 1997, *MNRAS*, 288, 404
 Hurwitz, M., Bowyer, S., & Martin, C. 1991, *ApJ*, 372, 167
 Jarvis, J. F., & Tyson, J. A. 1981, *AJ*, 86, 476
 Koo, D. C. 1986, *ApJ*, 311, 651
 Lanzetta, K. M., Wolfe, A. M., & Turnshek, D. A. 1995, *ApJ*, 440, 435
 Leitherer, C. 1999, in *IAU Symp. 186, Galaxy Interactions at Low and High Redshift*, ed. J. E. Barnes & D. B. Sanders (London: Kluwer), 243
 Lilly, S. J., Cowie, L. L., & Gardner, J. P. 1991, *ApJ*, 369, 79
 Lilly, S. J., Le Fèvre, O., Hammer, F., & Crampton, D. 1996, *ApJ*, 460, L1
 Loveday, J., Peterson, B. A., Efstathiou, G., & Maddox, S. J. 1992, *ApJ*, 390, 338
 Madau, P., Ferguson, H. C., Dickinson, M. E., Giavalisco, M., Steidel, C. C., & Fruchter, A. 1996, *MNRAS*, 283, 1388
 Madau, P., & Pozzetti, L. 2000, *MNRAS*, 312, L9 (MP00)
 Madau, P., Pozzetti, L., & Dickinson, M. 1998, *ApJ*, 498, 106
 Maeder, A. 1992, *A&A*, 264, 105
 Magorrian, J., et al. 1998, *AJ*, 115, 2285
 Malkan, M. A., & Stecker, F. W. 1998, *ApJ*, 496, 13
 Marzke, R. O., da Costa, L. N., Pellegrini, P. S., Willmer, C. N. A., & Geller, M. J. 1998, *ApJ*, 503, 617
 Metcalfe, N., Shanks, T., Fong, R., & Jones, L. R. 1991, *MNRAS*, 249, 498
 Metcalfe, N., Shanks, T., Fong, R., & Roche, N. 1995, *MNRAS*, 273, 257
 Miralda-Escude, J., & Ostriker, J. P. 1990, *ApJ*, 350, 1
 Mushotzky, R. F., Cowie, L. L., Barger, A. J., & Arnaud, K. A. 2000, *Nature*, 404, 459
 Mushotzky, R. F., & Loewenstein, M. 1997, *ApJ*, 481, L63
 O’Neil, K., & Bothun, G. 2000, *ApJ*, 529, 811
 Pagel, B. E. J. 1987, in *The Galaxy*, ed. G. Gilmore & B. Carswell (NATO ASI Ser. C, 207; Dordrecht: Reidel), 341
 ———. 1997, *Nucleosynthesis and Chemical Evolution of Galaxies* (Cambridge: Cambridge Univ. Press)
 ———. 1999, in *Galaxies in the Young Universe II*, ed. H. Hippelein (Berlin: Springer), 140
 Pagel, B. E. J., & Tautvaisiene, G. 1997, *MNRAS*, 288, 108
 Partridge, R. B., & Peebles, P. J. E. 1967, *ApJ*, 148, 377
 Pei, Y. C., & Fall, S. M. 1995, *ApJ*, 454, 69
 Pei, Y. C., Fall, S. M., & Hauser, M. G. 1999, *ApJ*, 522, 604
 Persic, M., & Salucci, P. 1992, *MNRAS*, 258, P14
 Pettini, M. 1999, in *ESO Workshop: Chemical Evolution from Zero to High Redshift*, ed. J. Walsh & M. Rosa (Berlin: Springer), 233
 Pettini, M., Ellison, S. L., Steidel, C. C., & Bowen, D. V. 1999, *ApJ*, 510, 576
 Pettini, M., Smith, L. J., Hunstead, R. W., & King, D. L. 1994, *ApJ*, 426, 79
 Pettini, M., Steidel, C. C., Adelberger, K. L., Dickinson, M., & Giavalisco, M. 2000, *ApJ*, 528, 96
 Poggianti, B. M. 1997, *A&AS*, 122, 399
 Pozzetti, L., Madau, P., Zamorani, G., Ferguson, H. C., & Bruzual, A. G. 1998, *MNRAS*, 298, 1133
 Renzini, A. 1997, *ApJ*, 488, 35
 Richstone, D., et al. 1998, *Nature*, 395, A14
 Salucci, P., Szuszkiewicz, E., Monaco, P., & Danese, L. 1999, *MNRAS*, 307, 637
 Sandage, A., & Perlmutter, J.-M. 1990, *ApJ*, 361, 1
 Silk, J., & Rees, M. J. 1998, *A&A*, 331, L1
 Smail, I., Hogg, D. W., Yan, L., & Cohen, J. G. 1995, *ApJ*, 449, L105
 Sprayberry, D., Impey, C. D., Irwin, M. J., & Bothun, G. D. 1997, *ApJ*, 482, 104
 Steidel, C. C., Adelberger, K. L., Giavalisco, M., Dickinson, M., & Pettini, M. 1999, *ApJ*, 519, 1
 Steidel, C. C., & Hamilton, D. 1993, *AJ*, 105, 2017
 Sullivan, M., Treyer, M. A., Ellis, R. S., Bridges, T. J., Milliard, B., & Donas, J. 2000, *MNRAS*, 312, 442
 Tinsley, B. M. 1972, *ApJ*, 178, 319
 Tinsley, B. M. 1977, *ApJ*, 211, 621
 ———. 1978, *ApJ*, 220, 816
 Treyer, M. A., Ellis, R. S., Milliard, B., Donas, J., & Bridges, T. J. 1998, *MNRAS*, 300, 303

- Tsujiimoto, T., Nomoto, K., Yoshii, Y., Hashimoto, M., Yanagida, S., & Thielemann, F.-K. 1995, *MNRAS*, 277, 945
- Tyson, J. A. 1988, *AJ*, 96, 1
- Valdes, F. 1982, Faint Object Classification and Analysis System, KPNO Internal Pub.
- Väisänen, P. 1996, *A&A*, 315, 21
- van der Marel, R. P. 1999, *AJ*, 117, 744
- Weir, N., Djorgovski, S., & Fayyad, U. M. 1995, *AJ*, 110, 1
- Williams, R. E., et al. 1996, *AJ*, 112, 1335
- Witt, A. N., Friedmann, B. C., & Sasseen, T. P. 1997, *ApJ*, 481, 809
- Wright, E. L. 2000, 2001, *ApJ*, 553, 538
- Wright, E. L., & Reese, E. D. 2000, *ApJ*, 545, 43
- Woolley, S. E., & Weaver, T. A. 1995, *ApJS*, 101, 181
- Yee, H. K. C., & Green, R. F. 1987, *ApJ*, 319, 28
- Yoshii, Y., & Takahara, F. 1988, *ApJ*, 326, 1

CORRECTIONS OF ERRORS IN “THE FIRST DETECTIONS OF THE EXTRAGALACTIC BACKGROUND LIGHT AT 3000, 5500, AND 8000 Å. I, II, AND III” (ApJ, 571; 56, 85, 107 [2002])

REBECCA A. BERNSTEIN,¹ WENDY L. FREEDMAN,² AND BARRY F. MADORE²

Received 2004 December 18; accepted 2005 June 3

ABSTRACT

We correct errors in a series of papers in which we described observations of the optical extragalactic background light (EBL). These errors pertain to the measurement of zodiacal light, given in the second paper of this series. Making these corrections leads to a net decrease of $0.5(\pm 0.6)\%$ in our zodiacal light measurement and a corresponding increase in the inferred extragalactic background light of roughly $0.5(\pm 0.6) \times 10^{-9}$ ergs s⁻¹ cm⁻² sr⁻¹ Å⁻¹. For comparison, the originally quoted EBL flux at 5500 Å was $2.7(\pm 1.4) \times 10^{-9}$ in the same units (1σ combined systematic and statistical uncertainty). We provide a detailed discussion of these errors and also discuss the evolution of this work prior to the 2002 papers. We note that corrections of the factual errors in our 2002 papers yield a result that is consistent with the results and errors quoted there. However, this is not intended to be a new or updated analysis, and it does not address some methodological objections which have been raised to our prior work.

1. INTRODUCTION

In Bernstein et al. (2002a, 2002b, 2002c; hereafter BFM1, BFM2, and BFM3, respectively), we described a measurement of the mean flux of the extragalactic background light (EBL) in a 5 arcmin² field of view. In that study, the EBL contribution was identified by measuring the total flux in the target field and subtracting from it the flux contributed by known foreground sources, namely diffuse Galactic light (DGL) and zodiacal light (ZL):

$$I_{\text{EBL}} = I_{\text{tot}} - I_{\text{ZL}} - I_{\text{DGL}}. \quad (1)$$

The total flux, I_{tot} , was measured from space using *Hubble Space Telescope* (HST) WFPC2 imaging in the *U*, *V*, and *I* bands and using HST FOS spectroscopy covering roughly 4000–7000 Å. The zodiacal light, I_{ZL} , was measured using ground-based spectrophotometry obtained at the du Pont 2.5 m telescope at Las Campanas Observatory (LCO) in Chile. The diffuse Galactic light, I_{DGL} , was estimated from a simple scattering model. The EBL values at 3000, 5500, and 8000 Å were measured to be $4.0(\pm 2.5)$, $2.7(\pm 1.4)$, and $2.2(\pm 1.0) \times 10^{-9}$ ergs s⁻¹ cm⁻² sr⁻¹ Å⁻¹, respectively.

The zodiacal light measurement, described in BFM2, is the only part of the experiment involving ground-based observations. The Earth’s atmosphere influences these observations through absorption, scattering, and airglow emission. Absorption and scattering cause “extinction” of the light in the target field; scattering causes a fraction of the light from the full, visible hemisphere of the sky to be added to the line of sight, and airglow is an additive foreground source produced in the atmosphere. The resulting night-sky spectrum observed from the ground (I_{NS}) was therefore described as a function of time (t), air mass (χ), atmospheric extinction (τ_{obs}), and wavelength (λ), as follows (eq. [3] of BFM2):

$$I_{\text{NS}}(\lambda, t, \chi) = I_{\text{target}} e^{-\tau_{\text{obs}}(\lambda)\chi} + I_{\text{scat}}(\lambda, t, \chi) + I_{\text{air}}(\lambda, t, \chi), \quad (2)$$

in which I_{scat} is the spectrum of light scattered into the line of sight and I_{air} is the airglow spectrum. To measure the zodiacal light in our experiment, we utilized the fact that the zodiacal

light is known to have a slightly reddened solar spectrum, in which the solar-strength Fraunhofer lines are preserved. The zodiacal light contamination can therefore be expressed as the product of a fiducial solar spectrum, $I_{\odot}(\lambda)$, and a scaling function, $C(\lambda)$, that varies roughly linearly with wavelength. The airglow spectrum, on the other hand, is not known to contain Fraunhofer features. We therefore identified the ZL flux by iteratively determining the scaling factor, $C(\lambda)$, for which the resulting residual airglow spectrum has the minimum correlation with the solar spectrum. We expressed the airglow spectrum as

$$I_{\text{air}}(\lambda, t, \chi) = I_{\text{NS}}(\lambda, t, \chi) - I_{\text{ZL}} \left[e^{-\tau_{\text{obs}}(\lambda)\chi} + \left(\frac{I_{\text{EBL}}(\lambda) + I_{\text{DGL}}(\lambda)}{I_{\text{ZL}}} \right) e^{-\tau_{\text{obs}}(\lambda)\chi} + \frac{I_{\text{scat}}(\lambda, t, \chi)}{I_{\text{ZL}}} \right], \quad (3)$$

in which the term $e^{-\tau_{\text{obs}}(\lambda)\chi}$ accounts for ZL flux lost from the beam due to extinction, and the scattered light term, I_{scat} , includes ZL, ISL (integrated star light), and DGL (diffuse Galactic light) as contaminating sources. As discussed in BFM2, we then needed a model for each scattering source over the visible spectrum in order to calculate the scattered light. To eliminate the absolute flux of the ZL from the models, we expressed the scattered light from all sources as a fraction of the ZL in the target field, as implied by equation (3). We then combined the net ZL loss due to extinction with net ZL gain due to scattering to give an effective extinction, $\tau_{\text{eff}}(\lambda)$. This let us express the effect of the atmosphere on the ZL as a relative (multiplicative) correction. The absolute value of the ISL, DGL, and EBL remain in the calculation. However, the EBL and DGL terms were then dropped because they were not expected to have Fraunhofer features and so were not expected to impact the spectral measurement based on the strength of these features.³ We therefore

³ This is correct for the EBL; however the DGL can and does contribute Fraunhofer features, and its spectrum should be included as a contribution to the target field and as a source of scattering in the spectral measurement of the ZL. The strength of zodiacal Fraunhofer lines in the DGL is weaker than in the solar spectrum by a factor of 3, so that the impact on our measurement would be roughly $0.01 \times I_{\text{ZL}}$.

¹ University of Michigan, Ann Arbor, MI 48109.

² Carnegie Observatories, 813 Santa Barbara Street, Pasadena, CA 91101.

identified the ZL flux [expressed as $C(\lambda)I_{\odot}$] according to the equation

$$I_{\text{air}}(\lambda, t, \chi) = I_{\text{NS}}(\lambda, t, \chi) - C(\lambda)I_{\odot} \left[e^{-\tau_{\text{eff}}(\lambda)\chi} + \frac{I_{\text{scat}}^{\text{ISL}}(\lambda, t, \chi)}{I_{\text{ZL}}} \right]. \quad (4)$$

We correct errors in our (2002) papers regarding the dates of the Las Campanas Observatory (LCO) observations, a statement regarding the location of the Moon on those dates, and quantify the implications of these corrections. We also include a discussion of analysis errors which pertains to all unrefereed work prior to the (2002) papers (Bernstein et al. 1996; Bernstein & Madore 1997; Bernstein 1998, 1999a, 1999b); these were corrected before publication of BFM2 and lead to no corrections here. Some of these errors were noted by Mattila (2003). We adopt nomenclature consistent with that of our earlier work to allow clear discussion of what was done there. Throughout this paper, we abbreviate 10^{-9} ergs s^{-1} cm^{-2} sr^{-1} \AA^{-1} as cgs.

2. ERRORS IN EARLY ANALYSIS

Mattila (2003) has correctly noted that the analysis of the ground-based data as detailed in the unpublished thesis (Bernstein 1998) contained an incorrect treatment of atmospheric effects. In that early analysis, atmospheric scattering was not included as a contribution to the observed night sky spectrum. In addition, due to a programming error in a subroutine, an incorrect extinction correction was applied. The incorrect treatment of atmospheric scattering was identified by the referee and both errors were corrected before publication. In the unpublished thesis, prior to the correction of these two errors, the ZL was therefore calculated based on the expression (compare to eq. [4] above)

$$I_{\text{air}}(\lambda, t, \chi) = I_{\text{NS}}(\lambda, t, \chi) - C(\lambda)I_{\odot} e^{-[\tau_{\text{obs}}(\lambda) - \tau_{\text{obs}}(4600)]\chi}. \quad (5)$$

Over the wavelength range used in that analysis (4200–5100 \AA) and at the mean air mass of our observations ($\chi \sim 1.2$), the exponential term in equation (5) has values between 0.93 and 1.06, with an average value of 1.00. In effect, the data were analyzed with no scattering correction and an incorrect extinction correction.

In brief, the analysis in Bernstein (1998) involved preparing solar spectra appropriate to each observation using IRAF routines to resample in wavelength and to apply an extinction curve for the air mass of each observation. The zodiacal light solution is then a scaling value relative to these prepared fiducial solar spectra. The solar spectra, corrected for extinction, were compared with the corresponding LCO spectra to find the contribution of zodiacal light. These solar spectra were produced many times in the course of data reduction, because the extinction and sensitivity solutions were recalculated many times. A check was therefore included in a subroutine to confirm that the solar spectra were correctly prepared. That check involved multiplying the solar spectrum by $\exp[\tau_{\text{obs}}(4600)\chi]$ with $\tau_{\text{obs}}(4600) = 0.2$ mag per air mass, roughly removing the extinction correction. The error then occurred by passing the wrong vector back to the main program from the subroutine. The programming error was not identified until the anonymous referee pointed out the incorrect treatment of atmospheric scattering. For completeness, we note that Figure 4.4 in Bernstein (1998) does not show the final extinction solution used in the thesis. The correct extinction solution used in all versions is shown in BFM2. Table 2.9 in Bernstein

(1998), which lists values for I_{tot} , was also updated in the published papers.

When properly treated, the scattering and extinction are nearly equal in magnitude but opposite in sign, and so they cancel to a high degree (to about 0.5% averaged over wavelength and air mass), giving the same result as the original analysis to within the accuracy of the measurements. The cancellation of the scattering and extinction terms in the proper analysis can be seen in the following quantitative example. At 4600 \AA and at our mean air mass (as given above), the extinction coefficient (Fig. 29 of BFM2) is $\tau_{\text{eff}}(4600) = 0.042$ mag per air mass and, accordingly, $\exp[-\tau_{\text{eff}}(\lambda)\chi] = 0.955$. Over the spectral range 3900–5100 \AA and at the same air mass, the net flux gained from scattered ISL is in the range 10–17 cgs. At 4600 \AA , the ISL scattered flux is 12.5 cgs. The ISL contribution impacts our ZL measurement to the degree that it contributes to the strength of the Fraunhofer lines in the observed night-sky spectrum; however, those features are only 10% to 40% as strong in the scattered ISL as in the ZL over the range 3900–5100 \AA , and 30% to 40% as strong around 4600 \AA (see Figs. 29 and 30 of BFM2). The scattered ISL therefore contributes +4.4 cgs (=12.5 cgs \times 0.35) to the solution, or $0.040 \times I_{\text{ZL}}$ (given that I_{ZL} is roughly 110 cgs.) The term in square brackets in equation (4) is therefore nearly unity (0.995 for this example). At higher air masses and shorter wavelengths, scattered flux (I_{scat}) and extinction (τ_{eff}) both increase. At smaller air masses and longer wavelengths, they both decrease. In either case, the term in square brackets in equation (4) is still nearly unity. In other words, the net loss due to extinction and the net gain due to scattering are synchronized and cancel to a level that is much smaller than the uncertainty in identifying the ZL flux contribution in the 16 spectra used in this analysis, which have an rms scatter of 2.3%. Because of this cancellation, statistically indistinguishable results were obtained in the early (Bernstein 1998) and published (BFM2) versions of the analysis. Note that the similarity between the net effects of atmospheric scattering and extinction alone are coincidental, and would likely not occur along lines of sight where the ZL in the target field is much brighter or fainter. They are also, of course, dependent on the parameters used to calculate the scattering model, which are documented explicitly in BFM2.

In the early analysis, no change in $C(\lambda)$ with wavelength was detected because the incorrect extinction correction masked the reddening of the ZL relative to the Sun. Because no color term was detected, several broad bandpasses were used. In the published version, an increase in $C(\lambda)$ with wavelength was identified, consistent with the reddened color of the ZL relative to the solar spectrum. Narrow bandpasses focused on the solar features were then used to help identify this trend.

3. DATES OF GROUND-BASED OBSERVATIONS

The dates of the ground-based observations were incorrectly recorded in the unpublished thesis and were subsequently transcribed by R. A. B. from there into the published papers. The original observing logs and the records of the observatory show that the correct dates of the run were the local-time nights of 1995 November 23/24 through November 27/28 (5 nights total). The last night of the run was used for imaging. Data from the first and third nights were not used because of weather and mechanical problems, as described in Bernstein (1998) and BFM2. The spectra cited and analyzed in BFM2 were therefore taken on nights 2 and 4 of the run, having local-time dates 1995 November 24/25 and 26/27. The corresponding UT dates were 1995 November 25 and 27. The incorrect dates affect the application of the zodiacal light measurement to the *HST* observations at the level of 0.2%

TABLE 1
CORRECTIONS TO CALCULATED ZODIACAL LIGHT

Issues for ZL Result	BFM2	Current Version	Multiplicative Change	Term(s) Affected	ΔI_{ZL} ($\times I_{ZL}$)
Shift in ZL (Nov 25, 27–Nov 29) (§ 3.1).....	...	–0.2 cgs	–0.002 (± 0.006)
Date used in scattering calculation (§ 3.2).....	Nov 29	Nov 25, 27	0.966, 0.96	$\tau_{\text{eff}}, I_{\text{scat}}(\text{ISL})$	<0.001
Exposure 1995 Nov 27 UT 3:10 (§ 4).....	included	excluded	–0.003
Cumulative change					–0.005 (± 0.006)

(although with significant uncertainty) and also affect the scattering calculations at the level of $<0.1\%$. We describe and quantify these two effects below.

3.1. Relevance for HST Observations

The *HST* observations analyzed in BFM1 were executed on the UT nights of 1995 November 29 and December 16–17. Ground-based observations were assigned and scheduled by the time-allocation committee about 1 year earlier. As stated in the abstract of BFM1, the observations were designed to occur contemporaneously with one of the sets of *HST* observations, but they were not executed simultaneously.

To get an idea of what the change in the ZL value might be between our LCO observations on 1995 November 25/27 and the *HST* observations on 1995 November 29, we can look at data in the literature and our own *HST* data. From 1995 November 29 to December 16/17, the *HST* WFPC2 and FOS data *both* showed a 2% decrease in the mean surface brightness of the EBL target field. As discussed in BFM1 and BFM2, this difference is what would be expected in sign and magnitude as the heliocentric longitude ($\lambda - \lambda_{\odot}$) of the target field goes from about 150° on 1995 November 29 to 130° on December 16/17. One expects this small decrease in intensity because the ZL is slightly brighter in the antisolar direction ($\lambda - \lambda_{\odot} = 180^{\circ}$) and has a broad minimum at $\lambda - \lambda_{\odot} = 130^{\circ}$.

For comparison, several data sets are available in the literature. The only all-sky measurements of the ZL surface brightness are from the ground. Of these, the most reliable are those tabulated by Levasseur-Regourd & Dumont (1980, hereafter LRD80) from their 1964–1975 observations at Tenerife Observatory. That data set is reproduced in Leinert et al. (1998), where it is updated with space-based values within 30° of the Sun. Although these data are ground-based and subject to scattering corrections, they are in good agreement with space-based results, as discussed in LRD80, Leinert et al. (1998), and BFM2. Between $\lambda - \lambda_{\odot} = 150^{\circ}$ and 130° and ecliptic latitude 31° – 35° , the data tabulated in LRD80 show a -6% change in the ZL flux. At these latitudes, data are also available from several other sources. As compared and discussed in Leinert et al. (1981) and Leinert et al. (1998), Frey et al. (1974) find a change of about $+2\%$ over these same angles, and the *Helios* space probes (Leinert et al. 1981, 1982) find a change of -1% . These three published results are in good agreement to within the errors of any of the measurements, which are of the order of 5% – 10% .

To be conservative in estimating the change in the ZL between 1995 November 29 and December 16/17, we simply average the values discussed above (-2% , -6% , $+2\%$, -1%) to obtain -1.7% , with a standard deviation of 3.3% . As the errors are probably systematic, the standard deviation may be more indicative of the uncertainty than the error in the mean. We then estimate that the change in the zodiacal light between November 25/27 LCO observations ($\lambda - \lambda_{\odot} = 153$ and 151) and November 29

for *HST* observations ($\lambda - \lambda_{\odot} = 149$) should be $-0.2(\pm 0.3)\%$ (i.e., slightly *fainter* on the 29th). To conservatively allow for any systematic uncertainties between the data sets, we double this error bar to $\pm 0.6\%$. We include this offset in the summary in Table 1.

3.2. Relevance for Scattering Calculations

Because of the transcription error in the dates of the observations, the scattering calculations in BFM2 were performed for the wrong date, namely, 1995 November 29 rather than November 25 and 27. The sky visible at a particular UT time shifts by roughly 1° per day. However, the target field and all sources of scattering obviously move in consort, so that the scattering calculated for a given zenith angle of the target is correct on any date. The one source that does not move in consort is the Moon; however, any spectrum affected by moonlight should not be included in the analysis (see § 4), and so the Moon is not included in the calculation of scattered light from extraterrestrial sources. The only change in the scattering calculations between November 25, 27, and 29 is therefore caused by the fact that the target field will rise 4 minutes earlier on each successive night. The scattering calculations for UT 2:00 on November 29 are therefore correct for UT 2:16 on November 25, and UT 2:08 on November 23. The net change in the scattered ZL and ISL for the largest difference in timing (16 minutes) is very small. Moreover, as illustrated in § 2, the net effect of the atmosphere (scattering and extinction of ZL, and scattering of ISL) nearly cancels at every zenith angle. For that reason, the change over 8 or 16 minutes is not detectable.

To illustrate this quantitatively, we note that the mean change in the effective extinction (Fig. 25, BFM2) is smaller by an average of 0.0013 mag per air mass between a given UT time and 16 minutes earlier. This translates into a fractional change of 0.03 in τ_{eff} . Using the mean air mass, $\chi = 1.2$, this corresponds to an increase in the net ZL by a factor of 1.0015 . As the scattered ISL gets brighter with increasing UT time, the scattered ISL would be correspondingly fainter by about 4% over that same time period (16 minutes earlier), and would decrease the strength of the ISL spectral features by the factor $0.998 (= 0.04 \times 0.35 \times 12.5 \text{ cgs}/I_{ZL})$. The net change with time is then $0.998 \times 1.0015 = 0.9995$, which is not significant. Nevertheless, for completeness, we list this term, and all other corrections discussed here, in the summary in Table 1.

4. LOCATION OF THE MOON

The LCO data were obtained by R. A. B. and took place several days after new Moon. Each night, as the Moon was setting, the open-dome time was used to observe bright, standard stars for calibration. Observations of the EBL target field began as the Moon approached the horizon. The general, but quantitative, statement in BFM2 that the Moon was at least 14° below the horizon during all but one exposure is incorrect. The correct

TABLE 2
LOCATION OF THE CRESCENT MOON DURING INDIVIDUAL EXPOSURES

Date (UT)	Start Time (UT)	Exposure Time (s)	Target Field Zenith Angle (deg)	Lunar Position Zenith Angle (deg)	Predicted Moonlight (% ZL)
1995 Nov 25.....	2:18	900	18.3–15.4	97.8–100.0	<1
1995 Nov 25.....	2:34	1800	15.2–10.4	100.9–106.3	...
1995 Nov 25.....	3:54	1800	10.5–15.4	114.8–119.4	...
(1995 Nov 27).....	(2:37)	(1800)	(13.3–9.4)	(81.7–87.8)	(~60)
1995 Nov 27.....	3:10	1800	9.1–9.8	88.4–94.0	~11
1995 Nov 27.....	3:41	1800	10.0–14.4	94.7–99.7	<1
1995 Nov 27.....	4:14	1800	15.0–20.9	101.3–106.3	...
1995 Nov 27.....	4:48	1800	21.7–28.1	106.9–112.4	...

statement is that one exposure that was used in the analysis began as the Moon was still setting (UT 03:10 on 1995 November 27); all other exposures used in the analysis were taken with the Moon below the horizon by several degrees. The times of the first few exposures and the corresponding position of the Moon during those exposures are given in Table 2 for all spectra taken until the Moon was more than 22° below the horizon on November 25 and 27. The spectra from these exposures are plotted in Figure 1.

Because of its high mean flux level, it was clear to us that the exposure beginning at UT 02:37 (Fig. 1, *open square*) was affected by moonlight, and for that reason it was not used in the analysis in BFM2. The Moon contributes exponentially less light with time after passing below the horizon (like the Sun at sunset). The remaining exposures were not obviously affected and

were therefore included in the subsequent analysis. We now consider what the impact of the Moon might have been on the included spectra.

To obtain a theoretical estimate of the scattered moonlight that might influence each exposure, we can use the scattering model described in BFM2. These estimates are given in Table 2 as a fraction of the ZL flux in the target field. Simpler models for moonlight sky brightness, such as that implemented by Skycalc v5,⁴ give consistent values at zenith angles smaller than about 85° , but yield higher values for the sky brightness very near the horizon. (These models do not predict the moonlight below the horizon; see Krisciunas & Schaefer [1991] for a discussion of the model implemented in Skycalc v5 and its uncertainties.) For the lunar phase and angular distance of the target from the Moon ($\sim 90^\circ$ on 1995 November 27), the estimated moonlight flux is negligible ($\ll 1\%$) by the time the Moon reaches a zenith angle of 98° .

We can also obtain an empirical estimate of the scattered moonlight in each exposure by simply comparing their mean fluxes. For the exposure beginning at UT 02:37 (which was clearly affected by moonlight and was *not* used in the analysis), the scattered moonlight is estimated to be about $0.60 \times I_{ZL}$ at 4600 \AA . The ZL accounts for roughly two-thirds of the night sky flux (see Fig. 9, BFM2), so that this spectrum is predicted to be about 40% brighter due to moonlight than spectra taken later. This is generally consistent with the empirical mean flux of the spectrum, which appears to be about 43% brighter than later spectra (Fig. 1, *open square*). For the exposure beginning at UT 03:10 (1995 November 27), the scattered moonlight is estimated to be $0.11 \times I_{ZL}$, implying that the mean flux for this spectrum should be about 8% higher than later spectra. The flux of this spectrum appears to be about 5% higher than the mean (Fig. 1, *open circle*), which is again generally consistent to within the accuracy of the scattering models at very high air masses. Note also that there is about 5% peak-to-peak variation in the mean flux of spectra that are not influenced by moonlight. This is presumably due to changes in atmospheric effects (changes in airglow, changes in extinction with air mass, and changes in scattered starlight and diffuse Galactic light). For this reason, the spectrum at UT 03:10 did not obviously appear to be problematic.

We conclude from the predicted and empirical fluxes of the spectra discussed above that the spectrum taken at UT 03:10 was probably affected by moonlight, and so we recalculate the final result without it. The ZL value derived from that exposure alone is 113 ± 3 (1σ), which is about 3%–4% higher than the mean

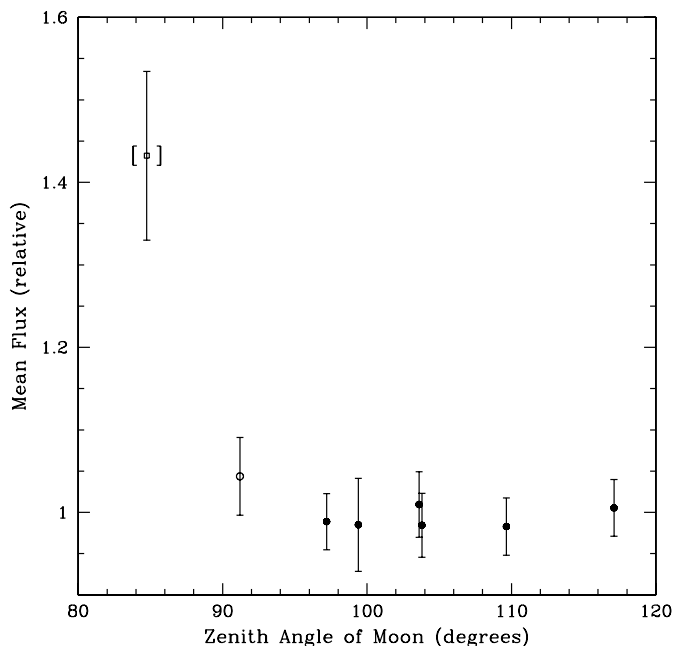


Fig. 1.—Mean flux of each exposure listed in Table 2 as a function of the average lunar position during the exposure. Circles indicate the mean flux of the seven spectra included in the analysis in BFM2, normalized by their combined mean. The open circle corresponds to the spectrum that was probably affected by moonlight and that we are now excluding from the analysis. The point marked by the open square and enclosed in brackets indicates the mean flux of the one exposure listed in Table 2 that was *not included* in the analysis of BFM2; this point is normalized by the same value as the other seven. To indicate the variability of the spectra as a function of wavelength, the error bars show the standard deviation of the difference between each spectrum and the mean of the seven analyzed spectra. These differences are due to changes in the relative contributions of airglow, scattered light, and ZL from the target field.

⁴ Skycalc v5.0 is available at <http://nfo.edu/master2/skycalc.v5.c> (J. Thorstensen, 2001).

(see Figs. 12 and 13, BFM2). Excluding this data point, the final ZL result (based on the average of 16 observations) is lower by 0.3%, which is roughly 1/2 the quoted statistical uncertainty and 1/4 the systematic uncertainty. The effect of excluding this exposure from the analysis is included in the summary in Table 1.

5. SUMMARY

We have presented corrections to the published results (BFM1, BFM2, BFM3), including the dates of the ground-based observations, the location of the Moon during each exposure, and the quantitative impact of these corrections. In addition, we have explicitly documented corrections made to the analysis between the unpublished thesis (Bernstein 1998) and published versions of this work (BFM2). The measured value of the ZL decreases by

$0.5(\pm 0.6)\%$, or $0.5(\pm 0.6)$ cgs, as a result of these changes. For comparison, the quoted measurement uncertainties in BFM2 are 0.6% (statistical) and 1.1% (systematic). The inferred EBL increases correspondingly by 0.1, 0.5, and 0.7 cgs in the U , V , and I bands. For comparison, the quoted 1σ uncertainties in each band were 2.5, 1.4, and 1.0 cgs, respectively. The corrections discussed here therefore yield a result that is consistent with the previously quoted result and errors; however, this is not intended to be a new or updated analysis.

We thank K. Mattila for his work and comments regarding these results.

REFERENCES

- Bernstein, R. A. 1998, Ph.D. thesis, California Institute of Technology, Pasadena
 ———. 1999a, in ASP Conf. Ser. 193, *The High-Redshift Universe: Galaxy Formation and Evolution at High Redshift*, ed. A. J. Bunker & W. J. M. van Breugel (San Francisco: ASP), 487
 ———. 1999b, in ASP Conf. Ser. 170, *The Low Surface Brightness Universe*, ed. J. I. Davies, C. Impey, & S. Phillipps (San Francisco: ASP), 341
 Bernstein, R. A., Freedman, W. L., & Madore, B. F. 1996, *BAAS*, 189, 1308
 ———. 2002a, *ApJ*, 571, 56 (BFM1)
 ———. 2002b, *ApJ*, 571, 85 (BFM2)
 ———. 2002c, *ApJ*, 571, 107 (BFM3)
- Bernstein, R. A., & Madore, B. F. 1997, in *HST and the High Redshift Universe*, ed. N. R. Tanvir et al. (Singapore: World Scientific), 57
 Frey, A., Hofmann, W., Lemke, D., & Thum, C. 1974, *A&A*, 36, 447
 Krisciunas, K., & Schaefer, B. 1991, *PASP*, 103, 1033
 Leinert, Ch., Richter, I., Pitz, E., & Planck, B. 1981, *A&A*, 103, 177
 Leinert, Ch., Richter, I., Pitz, E., & Hanner, M. 1982, *A&A*, 110, 355
 Leinert, Ch., et al. 1998, *A&AS*, 127, 1
 Levasseur-Regourd, A. C., & Dumont, R. 1980, *A&A*, 84, 277 (LRD80)
 Mattila, K. 2003, *ApJ*, 591, 119